Brain, Behavior, and Immunity 110 (2023) 245–259

Contents lists available at ScienceDirect

Brain Behavior and Immunity

journal homepage: www.elsevier.com/locate/ybrbi

Full-length Article

Real-time mechanisms of exacerbated synaptic remodeling by microglia in acute models of systemic inflammation and tauopathy

Carla Cangalaya [a,b,c], Susanne Wegmann [d], Weilun Sun [a], Lisa Diez [d], Anna Gottfried [b], Karin Richter [b], Stoyan Stoyanov [a], Janelle Pakan [a,e,g], Klaus-Dieter Fischer [b], Alexander Dityatev [a,f,g,*]

[a] German Center for Neurodegenerative Diseases (DZNE), Magdeburg, Germany
[b] Institut für Biochemie und Zellbiologie, Otto-von-Guericke-University, Medical Faculty, Magdeburg, Germany
[c] ESF International Graduate School on Analysis, Imaging and Modelling of Neuronal and Inflammatory Processes, Magdeburg, Germany
[d] German Center for Neurodegenerative Diseases (DZNE), Berlin, Germany
[e] Institute of Cognitive Neurology and Dementia Research, Otto-von-Guericke University, Magdeburg, Germany
[f] Medical Faculty, Otto-von-Guericke University, Magdeburg, Germany
[g] Center for Behavioral Brain Sciences (CBBS), Magdeburg, Germany

ARTICLE INFO

Keywords:
Microglia
Synapse
Spine turnover
Spine elimination
Synaptic remodeling
Spine head filopodia
C1q
C3
C3R
CD68
tau
Alzheimer's disease

ABSTRACT

Remodeling of synapses by microglia is essential for synaptic plasticity in the brain. However, during neuroinflammation and neurodegenerative diseases, microglia can induce excessive synaptic loss, although the precise underlying mechanisms are unknown. To directly observe microglia-synapse interactions under inflammatory conditions, we performed *in vivo* two-photon time-lapse imaging of microglia-synapse interactions after bacterial lipopolysaccharide administration to model systemic inflammation, or after inoculation of Alzheimer's disease (AD) brain extracts to model disease-associated neuroinflammatory microglial response. Both treatments prolonged microglia-neuron contacts, decreased basal surveillance of synapses and promoted synaptic remodeling in response to synaptic stress induced by focal single-synapse photodamage. Spine elimination correlated with the expression of microglial complement system/phagocytic proteins and the occurrence of synaptic filopodia. Microglia were observed contacting spines, then stretching and phagocytosing spine head filopodia. Thus, in response to inflammatory stimuli microglia exacerbated spine remodeling through prolonged microglial contact and elimination of spines 'tagged' by synaptic filopodia.

1. Introduction

Microglia, the resident macrophages of the central nervous system (CNS), play a crucial role in maintaining CNS homeostasis (Kettenmann et al., 2011). As a result of infection or disease, microglia alter their physiological state and function (Hammond et al., 2019; Streit et al., 2004). This response has been suggested to play a role in synaptic remodeling during development (Wu et al., 2015), and under neuroinflammatory conditions (Kettenmann et al., 2013; Krukowski et al., 2021; Salter and Stevens, 2017). For example, following peripheral exposure to lipopolysaccharide (LPS) (Andersson et al., 1992), an acute increase in microglial phagocytic activity (Akiyoshi et al., 2018; Savage et al., 2019) as well as delayed alterations in the density of synaptic proteins and spine loss (Kondo et al., 2011; Li et al., 2020; Manabe et al., 2021) have been reported. Moreover, pathology-triggered microglial phagocytosis is emerging as a contributing factor to early synaptic loss in neurodegeneration, for example in Alzheimer's disease (AD) and tauopathies (Salter and Stevens, 2017). Pathological changes in microglia morphology around amyloid plaques and fibrillary tangles coincide with a dramatic loss of synapses and spines, which has been documented both in *post mortem* human brain tissue (Tzioras et al., 2019) and in transgenic mouse models of AD and tauopathies (Meyer-Luehmann et al., 2008). In particular, it has been suggested that extracellular oligomeric Aβ and Tau may directly activate microglia, induce synaptic stress and reduce the density of spines (Nonaka and Nakanishi, 2019; Pickett et al., 2019). Cognitively, chronic or acute intraperitoneal exposure to LPS impairs learning and spatial memory in the Morris water maze test, and may increase Aβ generation similar to the changes that occur in AD (Lee et al.,

* Corresponding author at: German Center for Neurodegenerative Diseases (DZNE), Leipziger Str. 44, Haus 64, 39120 Magdeburg, Germany.
E-mail address: alexander.dityatev@dzne.de (A. Dityatev).

https://doi.org/10.1016/j.bbi.2023.02.023
Received 21 September 2022; Received in revised form 24 February 2023; Accepted 25 February 2023
Available online 9 March 2023

2008; Noh et al., 2014; Schreuder et al., 2017; Zhao et al., 2019). It has also been found that intracerebral delivery of human AD brain extracts triggers cognitive dysfunction in mice, characterized by deficits in the object recognition test (Lasagna-Reeves et al., 2012; Lam et al., 2022). Despite this evidence, fundamental questions about how systemic inflammation and AD influence microglia-dependent synaptic remodeling and synaptic loss *in vivo* remain unanswered. To counteract neurodegeneration, it is important to understand how microglia eliminate synapses and precisely which events precede this process.

In the current study we provide direct observations detailing the real-time mechanisms of synaptic remodeling by microglia in the mouse brain using *in vivo* two-photon microscopy. Two conditions triggering neuroinflammatory responses in the brain were employed, systemic LPS administration and local inoculation of tau-rich sarkosyl-insoluble AD brain material. Both conditions were associated with a microglial upregulation of phagosomal and complement markers (CD68, C3 and C3R), and led to disrupted surveillance of synapses by microglia. Targeted laser photoablation, which is known to release adenosine di- and tri-phosphate that attract microglia via activation of P2Y12 receptors (Haynes et al., 2006), was used to induce microglia-dependent synaptic remodeling. In both inflammatory contexts, we observed similarly enhanced spine remodeling, formation of spine-head filopodia (SHFs) and spine loss. Spine elimination of filopodia-'tagged' synapses included spine stretching and subsequent phagocytosis by microglia.

2. Materials and methods

2.1. Animals

On a C57BL/6 background, triple transgenic male mice were created which expressed CreERT2 and red fluorescent protein dtTomato in microglia under the control of the endogenous CX3CR1 loci (Yona et al., 2013) (RRIDs:# 007905 and 020940; Jackson Laboratory) and enhanced green fluorescent protein (EGFP) in excitatory neurons under the control of a adapted Thy1 promoter region (Feng et al., 2000) (RRID: # 007788; Jackson Laboratory). Animals were handled strictly in accordance with Directive 2010/63/EU, German law, and Saxony-Anhalt state's Ethical Committee on Animal Health and Care (license number: 42502-2-1346). Mice were kept at room temperature with a 12-hour light cycle and given food and water *ad libitum*.

2.2. Tamoxifen administration for induction of CreERT2 activity

To induce CreERT2-mediated recombination and labeling of microglia, P30-P45 male mice were intraperitoneally (i.p.) injected with five doses of tamoxifen (T5648, Sigma) (dissolved in corn oil at 20 mg/ml). Tamoxifen solution was freshly prepared the day before injections, and shaken overnight at room temperature and protected from light. Mice were injected with 2 mg Tamoxifen (0.1 ml volume; i.p. injections) once daily for 5 consecutive days (Cangalaya et al., 2020; Madisen et al., 2010).

2.3. LPS systemic administration

Ten 4.5-months-old male mice were randomly divided into two groups. Five mice were injected with two consecutive doses of LPS (Sigma-Aldrich, L4391-10x1mg; LPS Ecoli 0111-B4; i.p. injections) dissolved in phosphate-buffered saline PBS (1.5 mg/kg of body weight) and five mice were used for control injections (PBS) (Manabe et al., 2021; Velez-Perez et al., 2020). Mice were weighed immediately before injection, as well as 24 h, 48 h and 9 days after initiating the treatment (i.e., one week following the last LPS treatment) to assess the effect of LPS on body weight (the animal weights were stable). In addition to the 10 mice used for two-photon imaging, 3 mice were sacrificed at D1 and D2 following LPS injection for histological studies. In order to reduce the number of animals, we only used LPS-injected mice for each time point for the ex-vivo analysis. For statistical comparisons, we used the values from timepoint D0 (i.e. before LPS injection) as controls.

2.4. Preparation of sarkosyl-insoluble fractions from human brains

Human brain tissues from a histologically confirmed sporadic AD patient (Braak stage 5–6, male, 65 years old) and normal cognitive control (Braak stage 0, female, 57 years old) were used in this study. The extraction of sarkosyl-insoluble material from the human frontal cortex was done following a modified version of a previously reported procedure (Guo et al., 2016). For each purification, 3 g of brain tissue were homogenized. The resulting pellet after centrifugation at 120.000 g for 1 h at 4 °C was extracted with 0.1% of sarkosyl (Sigma). The pellet was carefully washed twice with PBS and then resuspended in PBS (0.1 ml/g tissue) using a 1 ml-syringe with a 27-G needle and further solubilized by brief sonication (20 pulses at ~0.5 s/pulse). Centrifugation at 150.000 g for 1 h at 4 °C re-pelleted the sarkosyl-insoluble fraction, which was then resuspended again in PBS (0.5-times the pre-centrifugation volume), sonicated with 60 pulses (~0.5 s/pulse), and spun at 2,000 g for 30 min at 4 °C to remove large debris. The final supernatant, enriched in sarkosyl-insoluble protein material, was stored at −80 °C. A protein concentration of 1.5 mg/ml (AD) and 0.9 mg/ml (control) was estimated from SDS-PAGE of bovine serum albumin (BSA) standard concentrations.

2.5. Fluorescent labeling of sarkosyl-insoluble fraction

AD and control sarkosyl-insoluble material was fluorescently labeled with Dylight405 dyes using NHS-ester chemistry (Thermofisher). Briefly, 100 µl protein material were mixed with 2 µl Dylight405-NHS dissolved in DMSO, incubated for 1 h at room temperature in the dark, and then dialyzed using a Pure-A-Lyzer Mini kit (MWCO 6000 Da, SIGMA) against 1 L of cold PBS overnight in the dark. A final Tau concentration of ~ 50 ng/ul in the labeled AD protein fraction was estimated from dot blots using an anti-total Tau antibody (DAKO, 1:2000) by comparison to known amounts of recombinant human Tau.

2.6. Immunoblotting of sarkosyl-insoluble fraction

For Western blot analysis of Dylight405-labeled sarkosyl-insoluble fractions from AD and control brain, 4 µl samples were boiled for 5 min in SDS-containing reducing sample buffer and loaded on 4–12% Bis-Tris SDS-PAGE gels (Invitrogen) in a MES buffer system. After transfer to a nitrocellulose membrane and blocking of the membrane in PBS containing 1% BSA, Tau protein and Aβ were detected by incubation with primary antibodies (rabbit anti-total Tau, DAKO, 1:5000; mouse anti-Aβ, 6E10, 1:1000) in blocking buffer overnight at 4 °C. Afterwards, the membrane was washed 3-times with PBS containing 0.05% Tween and then incubated with HRP-labeled secondary antibodies (anti-rabbit HRP, Sigma, 1:2000; anti-mouse-HRP, Sigma, 1:2000) for 1 h at room temperature. SeeBlue prestained (Invitrogen) mass weight marker was used to determine the protein sizes.

2.7. Surgical procedures

Surgery was carried out under aseptic conditions (Stoyanov et al., 2021). Mice were anesthetized with 4% isoflurane (Baxter, Germany) and placed in a stereotaxic apparatus (SR-6 M, Narishige Scientific Instrument Lab, Japan). An electric heating pad (ATC1000, World Precision Instruments, USA) was used to maintain the body temperature at 37 °C. Eye lubricant (Bepanthen, Bayer, Germany) was applied to prevent corneal desiccation. The isoflurane levels then were adjusted to 1.5–2% for anesthesia maintenance, the oxygen levels were set to 0.4 L/min using an isoflurane vaporizer (Matrx VIP 3000, Midmark, USA). The scalp was shaved and cleaned with 70% ethanol, an incision was made over the scalp and all soft tissues were retracted, the exposed

surface of the skull was cleaned with 10% povidone-iodine (Dynarex, USA) and 3% hydrogen peroxide solution (Sigma-Aldrich, Germany). Using a surgical stereoscope and an electric dental drill (Eickemeyer, Germany) a circular section of bone (4 mm in diameter) was removed centered at midline and 2 mm posterior from Bregma. A round glass coverslip (5 mm diameter, Thermo-Scientific) was mounted directly above the brain using cyanoacrylic glue (Pattex-Henkel, Germany). Finally, a rectangular head plate was placed over the glass coverslip and fixed by applying glue and dental acrylic cement (Paladur, Heraeus Kulzer, Germany) to also seal the implant and the tissue around the cranial window. The glue and cement were allowed to set for 5–10 min. The animals were then transferred to a warmed recovery cage and post-surgical analgesics (caprofen, 5 mg/kg of body weight, i.p.) were administered for three days.

2.8. Stereotaxic injection of sarkosyl-insoluble fractions from human brains

In this study we used surgical procedures modified from previous published protocols (Bolós et al., 2016). Tau-AD fractions (Tau concentration at 0.05 μg/μL), control-normal fractions (Tau concentration at 0.0 μg/μL) and vehicle solution (PBS) were intracerebrally injected into the retrosplenial cortex (RSC) of 3.5-month-old male CX3CR1-Cre-tdTomato × Thy-1-EGFP mice. 1 μl per hemisphere of each type of extract was infused into the RSC (Anterior-Posterior (AP): −2.0 mm; Medial-Lateral (ML): 0.5 mm; Dorsal-Ventral (DV): 0.5 mm) with a 35-gauge beveled needle attached to a 10 μl NanoFil syringe (World Precision Instruments, USA) using a Micro 4 MicroSyringe Pump Controller (World Precision Instruments, USA) at a speed of 100 nL/min at two different depths (~200 and 700 μm; 500 nL per site). Stereotaxic injections were performed before the implantation of the glass coverslip (see surgical procedures) under isoflurane anesthesia.

2.9. Two-photon microscopy

For fluorescence imaging, a Ti:Sapphire laser (Chameleon Vision II, Coherent) was used in combination with a multiphoton microscope (LSM 7 MP, Carl Zeiss, Germany). A 20x water immersion objective lens (Zeiss, N.A. = 1.0) was used to image the dysgranular region of the RSC (150–200 μm below the pial surface). Fluorescence signals were detected using BP-420–480, BP 500–550, and BP 565–610 filters. The wavelength of the two-photon laser was tuned to 900 nm for EGFP, 1040 nm for tdTomato and 600 nm wavelength for Alexa 405 for fast sequential acquisition frames. The average laser excitation power was kept at the lowest possible level to ensure a reasonable and stable signal-to-noise ratio across specimens and to prevent photobleaching and phototoxicity of microglia. Thirty minutes before imaging, mice were anesthetized with ketamine (i.p. injections 90 mg/kg body weight) and xylazine (18 mg/kg of body weight) in 0.9% NaCl solution (Sun et al., 2019). While undergoing the imaging procedures, an isoflurane/oxygen gas mixture of ~ 1% was used to maintain anesthesia. The body temperature was kept at 37C using a heating pad and the eyes were protected from dehydration using eye ointment during all imaging sessions (Bepanthen).

2.10. Laser photodamage

Laser photodamage was performed according to a previously published protocol (Cangalaya et al., 2020). Spine photodamage (Spine-PD) was performed by creating a 1 μm-long line (cut) at the selected segment of the spine using 150–200 mW laser power, 850 nm wavelength, 60 cycles (one second of irradiation for the chosen segment). Each spine must disappear within 30 min of recording to be considered a successful Spine-PD experiment. As with the Spine-PD experiments, Near-Spine-PD and Near-Bouton-PD were performed on the same day in neighboring fields of view using the same settings, however, the line scan was placed between the spine or axonal bouton at a distance of 0.5 um (without evidence of transient swelling of the dendritic or the axonal shafts). Zeiss Zen software was used to generate laser-photodamages in different fields of view with a separation of more than 200 μm identified with low magnification using the position module (20x objective, zoom factor: 1.5; 1024 × 1024 pixels; image size 292.01 μm × 292.01 μm). Before and after the photodamage, we acquired series of z-stacks every 10 min for a total of two hours, which were used to reconstruct dendrites or axonal branches in 3D (20x objective, zoom factor: 5; 1024 × 1024 pixels; 85.02 μm × 85.02 μm; a z-stack of 4–7 optical sections with 1 um z-spacing; 13 time-frames).

For Near-Spine-PD and Spine-PD, we used dendritic segments that averaged approximately 25 μm in length from secondary and tertiary dendritic branches with a minimum thickness of 2 μm and a maximum number of spines in one optical plane. For axonal branches, we selected segments that were approximately 40 μm long and had *en passant* boutons (EPBs) with an area of 1–2 μm^2 and without terminal boutons. The selection criteria for photodamaged spines and boutons were: well-defined structures, not contacted by microglia, and separated from surrounding spines and boutons. For longitudinal imaging of the same brain areas, the brain vasculature was used as an anatomical landmark.

2.11. Live imaging measurements

For each mouse, two–three replicas of spine photodamage were collected which consisted of time-lapse recordings of specific segments of dendrites before (baseline) and after the photodamage. Each time-lapse recording lasted 2 h (every 10 min), producing stacks of 5–10 z-slices, 13 time points, and three channels (EGFP, dtTomato, and Alexa 405). Based on these image stacks, a region of interest (ROI) of 51.48 μm × 25.74 μm was used for further image processing. Using ImageJ, the linear stack alignment with Sift and MultiStackReg Plugins (Thevenaz et al., 1998) as well as the dendritic branch were used to align stacks for each ROI.

Microglia-synapse contact: A maximum intensity projection was generated from the original z-stacks. With ImageJ, we used a macro and Coloc2 plugin to set a threshold to accurately measure the area of colocalization between EFGP and dtTomato channels in each time point (13 values) in μm^2. Later, these areas were divided by the area of the dendritic or axonal segment studied multiplied by 100. In addition, microglia-contacted spines or boutons were identified when more than 20% of the spine/bouton area was in contact with microglia in at least one slice of the z-stack and in at least one-time point (Weinhard et al., 2018).

Turnover: Original z-stacks and a 3D convolution viewer (ZEN software, Carl Zeiss) were used to manually perform the blinded count of spines and boutons by scrolling through the z-stacks. Spine and bouton turnover were calculated following a previously validated criterion (Holtmaat et al., 2005; Holtmaat et al., 2008; Holtmaat et al., 2006), and included the careful equalization of brightness and contrast across specimens during the acquisition stage to equilibrate signal-to-noise levels across specimens and days. For each of the 13 timepoints, lost and gained spines/boutons were identified and quantified based on the previous time-frame. Gained spines were defined as those that were >0.4 μm (five pixels) in length, and lost spines as those that were <0.4 μm and if their location to neighboring spines changed by ≥ 0.5 μm. To recognize gained axonal boutons, these structures need to be three times brighter than the axonal backbone. In order to score loss boutons, brightness had to be <1.3 times backbone brightness. Furthermore, at least two close boutons had to be separated by 2 μm in at least one z-plane. Turnover percentage (%) was defined as the cumulative number of spines/boutons that appeared (gained) and disappeared (lost) from one-time point to the next divided by the total number of spines/boutons from the previous time point to the time point analyzed (Holmaat et al., 2005; Cangalaya et al., 2020).

Filopodia measurements: Spine Head Filopodia (SHF) were described

as protrusions emerging from the spine head >0.5 μm in length and with a thickness of half or less than the spine head. In the case of boutons, filopodia were defined as processes longer than 1 μm in length, formed from EPBs (Wu et al., 2012). Filopodia from spines/boutons were characterized using three parameters: filopodia occurrence, size, and lifetime. Filopodia occurrence (%) was calculated as the number of spines/boutons that formed filopodia divided by the total number of spines and multiplied by 100. The maximal filopodia length (measured from the spine head to the tip of the SHF) observed during the 2 h of observation was expressed in μm and used for statistical comparisons. All filopodia events were traced over the two hours of observation and their lifetime was annotated in minutes.

Spine elimination: In this study, "spine elimination" refers to the disappearance of an existing or newly formed spine in a subsequent frame of an image. It may occur through retraction or engulfment. We defined "retraction of the spine" as the absence of EGFP-positive material internalized within the closest microglial processes and no evidence of its detachment from the dendritic branch during microglial contact. "Spine engulfment" describes the process in which microglia engulf EGFP-positive material from EGFP-positive spines. "Spine engulfment" by microglia was scored based on two criteria: the simultaneous disappearance of the neck of the spine and the presence of phagocytic EGFP-positive inclusions. In order to score these events, the Otsu method was used to delineate spines. The neck of the spine was considered as lost if the brightness of the space in between the dendritic branch and the phagocytic material was <1.3 times the brightness of the dendritic shaft. The phagocytic inclusions were defined as EGFP-positive bodies that accompanied the detachment of the spine and moved in the same direction as microglial processes being disconnected from dendrites. By using the Otsu's method in HSV color space, a color threshold was established to identify phagocytic inclusions within microglia bodies. While phagocytosis may affect the fluorescence of the EGFP since microglia lysosomes have an average pH of ~5.5 (e.g., Majumdar et al., 2007), even at this pH level, around 50% of EGFP fluorescence is retained (Patterson et al., 1997) and we observed minimal quenching of EGFP fluorescence within the sampling rate of our time-lapse imaging (see also engulphed EGFP+ puncta in Fig. 3A).

Morphological microglia analysis: Z-stack images were taken with the two-photon microscope (see above) at 1.5 μm using a 20X objective. Cell counting and morphology analysis were performed using ImageJ according to Young and Morrison's (2018) method. First, all z-stacks images were converted to maximum intensity projections. Second, although care was taken during acquisition to equalize signal-to-noise ratio across samples and days, to further equalize brightness and contrast, thresholding was applied and all images were binarized and unsharp mask and despeckle filters were applied to remove noise. For microglia morphology analysis, we used the ImageJ "analyse particles" command to calculate size, circularity and number of microglia soma. For manual assessment of these parameters, we used the "magic" selection tool to surround the cell bodies of microglia (Avignone et al., 2015). To obtain the number and length of branches, the images were skeletonized and measured using the AnalyzeSkeleton plugin in ImageJ (Arganda-Carreras et al., 2010). Branches containing ≤2 endpoints, <10 pixels (0.4 μm) in length were removed (Young and Morrison, 2018). A similar analysis was performed with confocal images (20 μm z-stack at 1.5 μm intervals, 20X objective) acquired at each ipsilateral and contralateral brain region.

2.12. Immunohistochemistry and confocal microscopy

Anesthetized mice (ketamine/xylazine; 90 mg/kg and 18 mg/kg body weight in 0.9% NaCl solution) were transcardially perfused with ice-cold PBS followed by 4% paraformaldehyde (PFA) in 0.1 M phosphate buffer, pH 7.4 (PB). After perfusion, the brains were removed from the skulls and were immediately post-fixed in 4% PFA in PB for 48 h at 4 °C. Following fixation, the brains were freeze-protected in 30% sucrose in PB at 4 °C (48 h), and subsequently stored at −80 °C until sectioning. Brains samples were coronally sectioned (40 μm) using a cryostat and stored at 4 °C in a cryoprotectant preservation solution (30% ethylene–glycol, 30% glycerol, 10% 0.2 M PB pH 7.4, in dH2O). For immunofluorescence assays, sections were first washed 3-times with PB and then pre-incubated for 1 h in a blocking solution (0.1% − 0.3% Triton X-100, 10% glycine, 5% normal goat or donkey serum). The free-floating sections were incubated for 72 h (4 °C) with primary reagents listed in Table 1 at 4 °C under agitation. Iba1, HT7, AT8 and Aβ antibodies were incubated under agitation for 48 h at 25 °C. Next slices were washed 3-times with PB, pre-incubated in blocking solution for 1 h (25 °C) and then incubated for 48 h (4 °C) with the appropriate secondary antibodies listed in Table 1. In the case of Iba1, HT7, AT8 and Aβ immunodetection, sections were directly incubated with the appropriate secondary antibody for 3 h under agitation (25 °C). After washing in PBS, sections were mounted on slides and embedded in Immu-Mount (Thermo-Scientific). Confocal laser scan images (Carl Zeiss LSM 700) were obtained using Achroplan 20x objective (N.A. = 0.4) and Plan-Neofluar 40×/1.34 objectives while keeping the laser intensity and detector gain settings consistent across specimens. Z-stacks of images were taken at 1.5 μm intervals, processed with ImageJ and displayed as maximum intensity projections for quantification.

Quantification of histochemical measurements: First, z-stacks were converted to maximum intensity projections and semi-automated thresholding was applied to all images to further standardize brightness and contrast across specimens. To measure the internalization of human tau or Aβ by microglia we identified the co-localized pixels between each marker and Iba-1 per microglia in ImageJ. A profile of pixels was generated using a customized ImageJ macro using the Otsu's method in HSV color space and color threshold. The quantification was using the default 'Analyze particles' plugin in ImageJ. The calculated area later was normalized by the area of each microglia and expressed as percentage.

Images were acquired with a confocal microscope (Carl Zeiss LSM 700) using a 63x objective (N.A. = 1.4) with 0.2-μm z-steps to determine synaptic engulfment by microglia (Schafer et al., 2014). ImageJ software was used to threshold and subtract the background from all fluorescent channels in z-stacks. Confocal images with z-stacks were utilized for 3D reconstruction using 3D viewer plugin (ImageJ) and Imaris software (Bitplane). Images were acquired using the same parameters as described for synaptic engulfment to assess C1q/C3 colocalization with spines and SHFs. ImageJ and SynapseCounter plugin (Dzyubenko et al., 2016) were used for consistent thresholding of all channels and to smooth the images to remove noise (Nguyen et al., 2020). Next, the colocalized areas were overlaid with skeletonized images of the Thy1 channel to obtain the number of spines colocalized with C1q or C3. Further confirmation was done by manually scrolling through the z-stack. Quantification was carried out on secondary and tertiary dendritic branches parallel to the optical plane (5–10 dendrites per mouse, average length = 78 μm, range = 39 – 134 μm).

2.13. Exploration of 3D electron microscopy images

To explore the connectivity between microglia and spines under physiological conditions, we used the IARPA MICrONS (https://www.iarpa.gov/index.php/research-programs/microns) dataset which spans a 1.4 mm × 0.87 mm × 0.84 mm volume of cortex in a healthy male young adult P87 mouse (Alexander Bae et al., 2021). We used the dataset from cortex65 (also called "minnie65"), which is the anterior portion of the cortical mm^3 of mouse visual cortex dataset. We merged the dataset cortical columns "Cell meshes" and "Microglia" available in MICRrONs Explorer. A random selection of three microglia cells was made from nine segments identified as microglia cells, and we manually examined direct contacts between these cells and SHF in MICRrONs Explorer.

As we could not identify any 3D EM dataset for AD or LPS, we used

Table 1
List of reagents and resources.

Reagent or resource	Source	Identifier
Antibodies		
Rabbit anti-Iba1	Wako	Cat# 019-19741, RRID: AB_839504
Mouse anti-human-tau (AT8) (recognizes the Tau phosphorylationed of tau at Ser202/Thr205)	Thermo Fisher Scientific	Cat# MN1020, RRID: AB_223647
Mouse anti-human-tau (HT7)	Thermo Fisher Scientific	Cat# MN1000, RRID: AB_2314654
Mouse anti-human Amyloid-beta (N), 82E1 (specific for human Amyloid beta)	IBL	Cat# 10303, RRID: AB_10707424
Rat anti-mouse-C3	Hycultec	Cat# HM1045, RRID: AB_533005
Rat anti-mouse-C3aR	Hycultec	Cat# HM3028, RRID: AB_10130173
Rat anti-mouse-CD68	Bio-Rad	Cat# MCA1957, RRID: AB_322219
Rabbit anti-C1q	abcam	Cat# ab182451, RRID: AB_2732849
Chicken anti-VGLUT1	Synaptic system	Cat# 135316, RRID: AB_2619822
Rabbit anti-activated Caspase-3	Cell signaling	Cat# 9661, RRID:AB_2341188
Guinea pig anti-Homer1	Synaptic system	Cat# 160004, RRID: AB_10549720
Mouse anti-FosB	abcam	Cat# ab11959, RRID: AB_298732
Chicken anti-NeuN	Millipore	Cat# ABN91, RRID: AB_11205760
Alexa Fluor™ 647-conjugated goat anti-rabbit	Invitrogen	Cat# A-21245, RRID: AB_2535813
Alexa Fluor™ 647-conjugated goat anti-mouse	Invitrogen	Cat# A-21235, RRID: AB_2535804
Alexa Fluor 647 AffiniPure donkey anti-rat IgG	Jackson	Cat# 712-605-153, RRID: AB_2340694
Alexa Fluor™ 405-conjugated donkey anti-guinea pig	Sigma Aldrich	Cat#SAB4600467, RRID: AB_2637046
Alexa Fluor™ 488-conjugated goat anti-chicken	Invitrogen	Cat#A-11039, RRID: AB_2534096
Alexa Fluor™ 647-conjugated goat anti-chicken	Invitrogen	Cat#A-32933, RRID: AB_2762845
Alexa Fluor 647 AffiniPure donkey anti-rat IgG	Jackson	Cat# 712-605-153, RRID: AB_2340694
Experimental models: Organisms/strains		
Gt(ROSA)26Sor$^{tm9(CAG-tdTomato)Hze}$	The Jackson Laboratories	Stock No: 007905 RRID: IMSR_JAX:007905
Cx3cr1$^{tm2.1(cre/ERT2)Jung}$	The Jackson Laboratories	Stock No: 020940 RRID: IMSR_JAX:020940
Tg(Thy1-EGFP)MJrs	The Jackson Laboratories	Stock No: 007788 RRID: IMSR_JAX:007788
Software and algorithms		
ImageJ (Fiji version)	NIH	https://imagej.net/Fiji RRID: SCR_002285
ZEN	Carl Zeiss Microscopy, LLC	https://www.zeiss.co m/microscopy/us/pro ducts/microscopesoftware/zen.html RRID:SCR_018163
R	R Foundation for Statistical Computing	https://www.R-project.org/ RRID:SCR_001905
Chemicals, peptides, and recombinant proteins		
LPS Ecoli 0111-B4	Sigma-Aldrich	Cat# L4391-10x1MG
Tamoxifen	Sigma-Aldrich	Cat# T5648
Pure-A-Lyzer Mini kit	Thermo Fisher Scientific	Cat# 69576
Isoflurane	Baxter	Cat# HDG9623
Paraformaldehyde	ROTH	Cat# P087.5
Paladur	Heraeus	Cat# 013199
Fluoromount	Sigma-Aldrich	Cat# F4680-25ML

the *H*01 dataset which spans 1.4 petabyte electron microscopy volume from the temporal lobe of the cerebral cortex of a patient with drug-resistant epilepsy (Shapson-Coe et al., 2021), as another inflammatory condition. We used the dataset from layer 3/4. We merged the dataset "Neurons" and "Microglia" available in *H*01 dataset. Three microglia were randomly selected from 27 identified microglia cells for manual inspection of direct contacts with SHFs in *H*01/Neuroglancer Explorer.

2.14. Statistics

We used RStudio 4.0.3 software to manage and analyze data. Data visualization was performed with the R-package ggplot2. GEE (R-packages: lmer4 and emmeans) was used to compare temporal profiles of microglia-synapse parameters between different treatment groups. Additionally, GEE was conducted based on an independent within-group correlation structure to calculate the interaction between time and treatment groups, followed by the Tukey's post-hoc test for multiple comparisons (Models: time as repeated measures, treatment as a fixed factor, time as a covariate, and their interaction treatment*time). Unpaired Generalized Linear Model (GLM) followed by Tukeýs post-hoc tests for multiple comparison were used to analyze data from ex-vivo specimens. In all cases that are reported as significant differences between groups, the p-value is < 0.05.

3. Results

To elucidate how microglia modify their response to inflammatory challenges in terms of synaptic remodeling *in vivo*, we used two approaches. First, we used intraperitoneal injections of LPS, which is a common systemic inflammation model (Andersson et al., 1992). Second, stereotaxic brain injections of sarkosyl-insoluble brain fraction from AD frontal cortex (Braak stage V-VI) (Tau-AD) were employed to mimic a neuroinflammatory environment similar to AD. To observe the dynamics of microglia-synapse interaction, we used triple-transgenic CX3CR1Cre/tdTomato × GFPM Thy-1 mice, in which a subpopulation of cortical neurons and microglia express fluorescent proteins, EGFP and tdTomato, respectively (Fig. 1A). Cranial windows were implanted above the retrosplenial cortex (RSC), as this brain region is an early-affected cortical region in AD. Two-photon time-lapse imaging of EGFP-positive synapses and tdTomato-positive microglia was performed for multiple hours and across days.

3.1. Microglial response to LPS and human AD extracts lead to internalization of postsynaptic protein in microglia

For LPS treatment, mice were randomly assigned to two groups, with 5 mice receiving two consecutive intraperitoneal doses of LPS (1.5 mg/kg) and 5 mice treated with vehicle as control using the same delivery schedule (Fig. 1A). As suggested by previous studies (He et al., 2020; Manabe et al., 2021), two consecutive doses of LPS induced microglial activation without signs of neuronal toxicity (Fig. 1B and Fig. S1A). Two-photon images of cortical synapses and microglia were acquired before LPS treatment (D0), and 24 h (D1) and 48 h (D2) after the first injection, as well as one week after the second LPS injection (W1). Each day, selected fields of view were followed using time-lapse imaging over multiple hours to monitor the dynamic morphological changes. After injection of LPS, microglia acquired an "activated/bushy" appearance (Fernández-Arjona et al., 2019), displaying morphological abnormalities 1–2 days post-injection (Fig. 1B): the total somatic microglial area increased (Vehicle: 28.85 ± 3.00 μm^2 vs LPS: 52.45 ± 4.03 μm^2, $p < 0.0003$) and the branch length decreased at D2 (Vehicle: 58.36 ± 3.83 μm vs LPS: 40.95 ± 4.17 μm, $p = 0.024$) (Fig. 1C). One week after the second LPS injection, these parameters of microglial morphology returned to control values (W1 in Fig. 1C; also Fig. S1B), indicating a recovery from the activation state as previously reported using LPS models (Akiyoshi et al., 2018; Manabe et al., 2021).

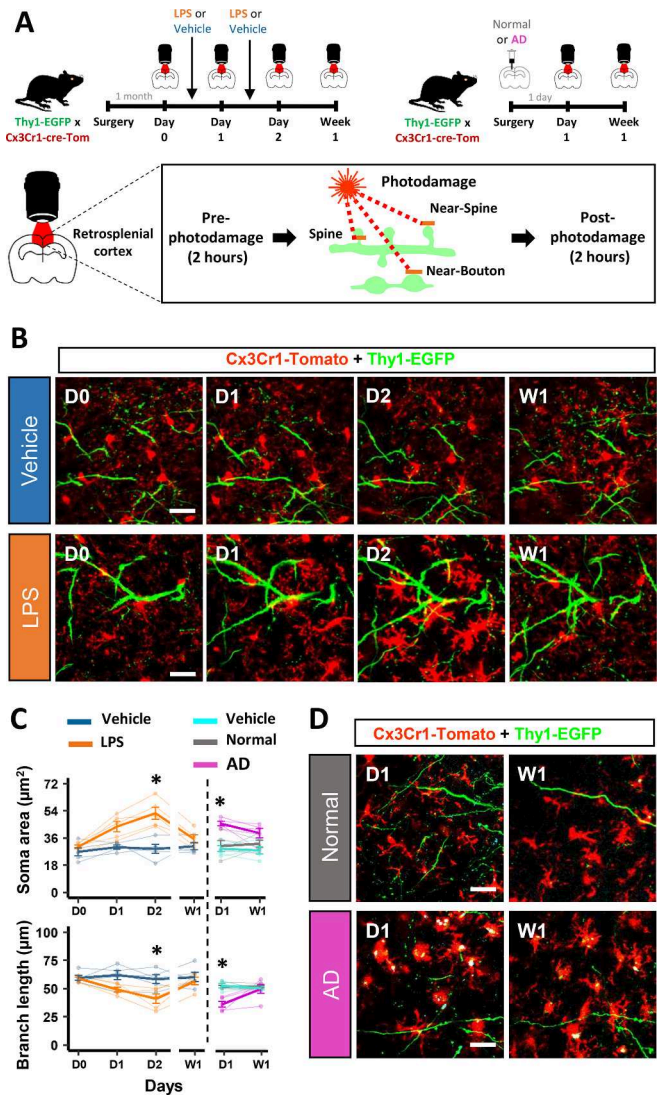

Fig. 1. Acute morphological changes of microglia after systemic administration of LPS and local inoculation of Tau-AD. (A) Experimental design to study neuroinflammation in CX3CR1-Cre-tdTomato x Thy-1-EGFP mice with tdTomato (red) expression in microglia and EGFP (green) expression in neurons, with a schematic representation of the sessions used to image microglia-neuron interactions pre-photodamage (baseline) and after photodamage in the same animal. Short horizontal bars (≈1 μm) illustrate locations of the photodamaged area. (B) In vivo two-photon microscopy time-lapse imaging shows alteration of microglia morphology from day zero (D0) to week one (W1) after LPS administration. Scale bars, 20 μm. (C) Quantitative analysis of microglial morphology. Bold lines show group mean ± SEM values, thin lines represent individual animals (n=5 mice per group). * $p < 0.05$, ** $p < 0.01$ for GEE posthoc pairwise comparison of LPS vs Control and Tau-AD vs Control on each particular day with the Tukey method. (D) In vivo two-photon microscopy time-lapse imaging shows alteration of microglia morphology on D1 and W1 after Tau-AD injection. White spots denote sarkosyl-insoluble material labelled by Alexa Fluor405 inside microglia bodies. Scale bars, 20 μm.

The course of microglia reactivity upon exposure to sarkosyl-insoluble AD and control brain fractions was examined in a similar way. Compared to non-demented control brain without Tau and Aβ pathology (Normal), the sarkosyl-insoluble fraction from AD brain (Tau-AD) was enriched in aggregated phosphorylated Tau and contained Aβ. To visualize the injection site, proteins in sarkosyl-insoluble in fractions from AD and control brains were fluorescently labeled by chemical coupling of AlexaFluor405. Five mice per group received an intracerebral injection of either control or AD brain fractions or vehicle solution (PBS) into the RSC (Fig. 1A). Similar to the results observed after LPS treatment, microglia exhibited an altered morphology following Tau-AD inoculation (Fig. 1D, S1B), including enlarged cell somata (Control: 30.75 ± 3.59 μm^2 vs Tau-AD: 45.64 ± 1.39 μm^2, $p = 0.005$) and shortened and thickened processes (Control: 51.83 ± 0.99 μm vs Tau-AD: 36.16 ± 2.65 μm, $p = 0.001$) (Fig. 1C). One week after the injection, microglia in Tau-AD-injected mice displayed a similarly ramified morphology as in control brain extract injected mice (Fig. 1C, S1B), with an increase in microglia recruitment to the injection site in both groups (Fig. S1B).

Because in vitro models have shown that microglia can rapidly internalize and degrade sarkosyl-insoluble Tau (Luo et al., 2015) and as the fraction isolated from postmortem AD brain was found to be enriched in hyperphosphorylated tau species and Aβ by western blotting (Fig. 2A-B), we investigated whether morphological changes of microglia were accompanied by Tau and Aβ internalization 24 h (D1) and one week (W1) after injection. Internalization of human Tau and Aβ was evident in D1 brain sections using a human Tau specific HT7 antibody (Fig. 2C-F). We also detected an increase in phosphorylated Tau with AT8 antibody within microglial cell bodies on D1 (Control: 0.03 ± 0.02 vs Tau-AD: 0.35 ± 0.09, $p = 0.0008$) (Fig. 2G). The amount of total human Tau and phosphorylated Tau (0.13 ± 0.05, $p = 0.01$) internalized by microglia was significantly lower one week after injection (Fig. 2G). These data indicate that the injection of Tau- and Aβ-rich insoluble AD brain material triggered microglial activation and Tau internalization at D1, which partially recovered to control levels one week after injection, likely due to degradation and digestion of the injected brain material.

To further characterize microglia activation in both models, immunofluorescent labeling of CD68, C1q, C3, and C3R was performed in brain sections of mice used for two-photon imaging. Immunolabeling of CD68-positive lysosomes inside microglia suggested upregulated phagocytic activity after treatment with LPS or inoculation of Tau-AD. CD68 fluorescence inside microglia was elevated after LPS treatment at D1 and D2, compared to baseline conditions (D0), which recovered after a week (Fig. S2A). After Tau-AD injection, microglial CD68 levels were significantly increased even after a week (Fig. S2A). In LPS treated animals, the fluorescence intensity of C3R and C1q in microglial somata increased (Fig. S2B-C) from D1 to D2, indicating the activation of the complement pathway. In Tau-AD animals, complement proteins appeared also highly upregulated at D1, with strongly elevated immunoreactivity of C3R, C3 and C1q both inside microglia and in the surrounding neuropil of the RSC (Fig. S2B-D). In accordance with previous observations that complement proteins and neuroinflammation are upregulated in AD and systemic inflammation mouse models (Dejanovic et al., 2018; Wu et al., 2019), these results confirm the high phagocytic activity of microglia in the imaged RSC regions. Next, we examined whether the increased expression of CD68, C1q and C3 also are associated to increased synaptic engulfment by microglia. We did not detect a significant accumulation of internalized presynaptic VGLUT-1 in microglia in either of the inflammatory contexts (Fig. S3A); however, LPS and AD brain extracts increased the engulfment of postsynaptic Homer-1 puncta by microglia on D2 (Vehicle: 0.55 ± 0.03 vs LPS: 2.63 ± 0.92, $p = 0.04$) and D1 (Normal: 0.91 ± 0.08 vs Tau-AD: 2.85 ± 0.79, $p = 0.019$) (Fig. S3A), indicating increased microglial internalization of postsynaptic dendritic spines.

3.2. LPS and Tau-rich AD brain extract disrupt basal levels of synapse surveillance by microglia

To investigate how the two inflammatory challenges alter the basal interaction of microglia with synapses, we imaged microglia and individual, randomly selected neuronal dendrites every 10 min for 2 h (2–3 dendrites per mouse; Fig. 1A, 3A) and across days. We defined physical microglia-spine interactions as those where microglial processes overlayed dendritic spines (yellow; Fig. 3A). Within a 2-hour interval, the

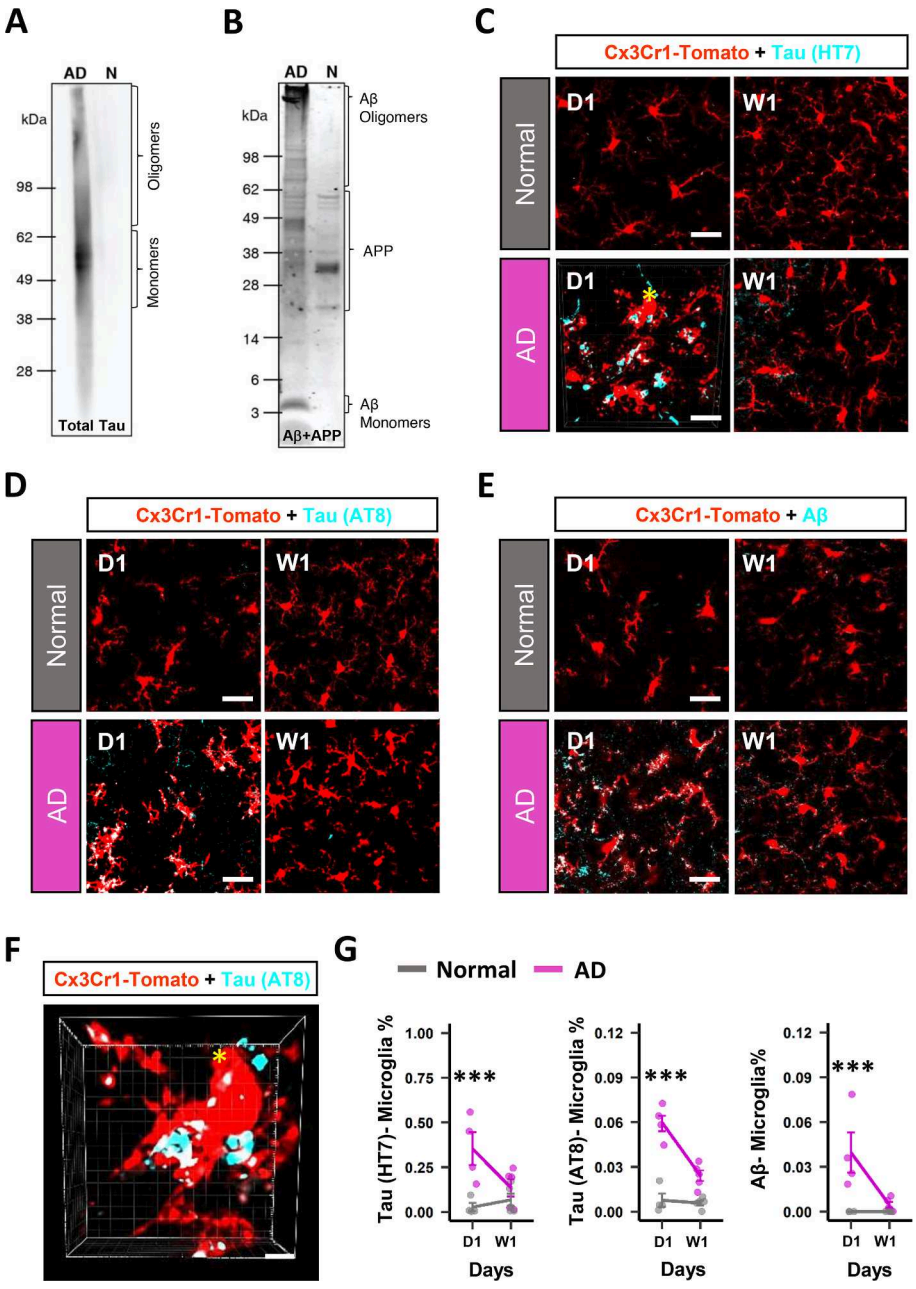

Fig. 2. Microglial internalization of human Tau-AD and Aβ. (A-B) Tau-AD extract was enriched in Tau and Aβ (Western blots on the right). (C-E) Intracerebral injections of Tau-AD extract into the mouse retrosplenial cortex (RSC) resulted in Tau and Aβ internalization by microglia 1 day (D1) and 1 week (W1) after injection (two-photon images show CX3CR1Cre/Tomato-positive microglia in red and Tau (HT7 or AT8 antibody) or Aβ in cyan). Yellow asterisk in C shows the microglia cell that was selected for 3D reconstruction in panel F. Scale bars, 20 μm. (F) Representative 3D reconstruction of high resolution images showing colocalization of HT7 and Cx3Cr1-Tomato signal in RSC 1 day after injection. Scale bars, 5 μm. (G) Plots show the quantification of HT7 and Aβ internalization area by microglia in the RSC normalized by microglia area. Group mean ± SEM values are shows, dots represent mean values per animal (Normal-D1 and AD-D1 groups: N=4 mice; Normal-W1 and AD-W1 groups: n=5 mice). * $p < 0.05$, ** $p < 0.01$, *** $p < 0.001$, GLM followed by post hoc Tukey's test.

contact time between microglia and individual dendritic spines in LPS treated (D2: Vehicle: 32.52 ± 3.07 min vs LPS: 47.93 ± 3.26 min, $p = 0.044$) and Tau-AD injected mice (D1: Normal: 22.25 ± 2.03 min vs Tau-AD: 36.95 ± 4.41 min, $p = 0.036$) was higher than in control injected animals (Fig. 3B). In contrast, the occurrence of microglial contacts with spines was significantly reduced in the LPS group at D1 (Vehicle: 35.14 ± 5.35% vs 16.90 ± 1.96% of all imaged spines, $p = 0.011$) and D2 (Vehicle: 35.24 ± 3.03% vs 19.67 ± 1.60%, $p = 0.045$) and in Tau-AD injected mice at D1 (Control: 28.19 ± 1.45% vs Tau-AD: 17.86 ± 2.26%, $p = 0.047$) (Fig. 3B). A week after the initial injections of LPS or Tau-AD, the contact changes in these groups were abrogated (Fig. 3B). Next, we examined whether mature, larger spines were contacted more by microglia, but no difference in spine size was found between microglia-contacted and non-contacted spines (Fig. S3B). Thus, in both inflammatory contexts, microglia showed abnormal surveillance of synapses, with reduced contact frequency but increased contact duration per synapse. Despite significant changes in contact dynamics, no difference in the basal turnover (% spines that appeared or disappeared over 2 h) was detected between the treatments (Fig. S3B), perhaps due to the low occurrence of these remodeling events (0–3 events) during the time-window of time-lapse recordings (2 h) in the limited area available for high-resolution observations.

3.3. *LPS and Tau-rich AD extract exacerbated synaptic turnover and spine loss following focal photodamage*

To be able to analyze the process of synaptic remodeling by microglia in a significant amount of remodeling events, we induced microglia-synapse interactions by focal laser damage of neurites (Cangalaya et al., 2020), which results in extracellular elevation in reactive oxygen species (ROS) (Cai and Tammineni, 2017; Keller et al., 2000), adenosine triphosphate (ATP) (Cai and Tammineni, 2017; Devi et al., 2006; Reddy and Beal, 2008), and phosphatidylserine (PtdSer) (D'Amelio et al., 2011). We previously adapted this approach to reproducibly introduce

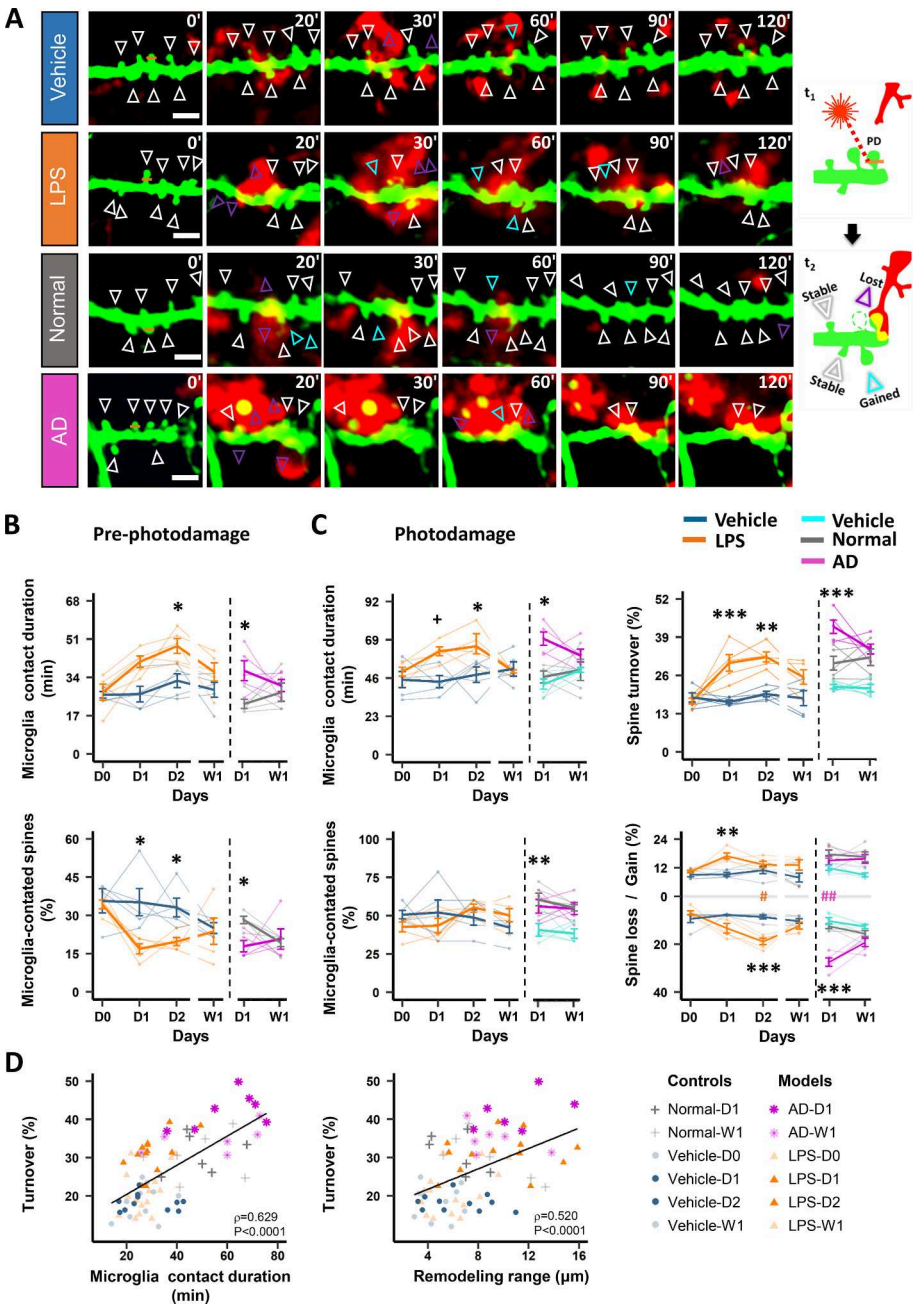

Fig. 3. Synaptic remodeling is exacerbated by prolonged contact of microglia after photodamage in both pathological conditions. (A) Representative time-lapse images to illustrate synaptic remodeling after photodamage of a single spine at 0, 20, 30, 60, 90 and 120 min: at day two (D2) following LPS and vehicle injections; and one-day (D1) post-injection of Tau-AD and Normal extracts. W1 timepoint is one week following the last treatment. Microglia are visualized in red and neurons in green, the contact area between both cells is visualized in yellow. Scale bars, 2 µm. Stable, gained and lost spines are indicated by white, cyan and purple arrows, respectively. (B) Baseline recordings were performed in selected dendritic branches every 10 minutes for 2 hours. Effects of LPS and Tau-AD injections on microglia contact duration (upper panel) and the number of microglia-contacted spines (lower panel). Bold lines show group mean ± SEM values, thin lines represent individual animals (n=5 mice per group). * $p < 0.05$, ** $p < 0.01$, *** $p < 0.001$, GEE posthoc pairwise comparison with Tukey method. (C) Time-course of microglia activation effects on microglia-neuron interaction and synaptic remodeling after photodamage (2-3 replicates per mouse). Pink and orange hash denote significant differences between Gained % and Lost % in the LPS group at D2 and the Tau-AD group at D1. Bold lines show group mean ± SEM values, thin lines represent individual animals (n=5 mice per group). $^{+}$ $p = 0.05$, * $p < 0.05$, ** $p < 0.01$, *** $p < 0.001$ for GEE posthoc pairwise comparisons (LPS vs vehicle and Tau-AD vs normal) with the Tukey method. (D) Scatter plots show that spine turnover and loss after photodamage correlate with microglia-neuron contact area and duration. Each symbol represents one photodamage experiment (n=5 mice per group), the solid line shows linear regression. ρ, Spearman coefficient of correlation. * $p < 0.05$, ** $p < 0.01$, *** $p < 0.001$.

photodamage at single synaptic sites and demonstrated that the resulting spine remodeling in the vicinity to the photodamage site requires microglia (Cangalaya et al., 2020). Here, we applied this approach for the controlled induction of focal synaptic stress to compare the otherwise rare microglial synaptic remodeling and microglia dynamics during 2-hour recording windows (Fig. 1A; Fig. 3A).

Following photodamage, we found an increased contact time between microglia and spines in LPS and Tau-AD treated animals compared to controls (D2: Vehicle: 48.03 ± 4.71 min vs LPS: 66.53 ± 6.09 min, $p = 0.0484$; D1: Vehicle: 46.65 ± 3.56 min vs, AD: 69.57 ± 4.03 min, $p = 0.013$) (Fig. 3A, 3C, Videos S1–S4). Tau-AD injected animals also showed a decrease in contacted spines (% of all imaged spines; Fig. 3C). These changes returned to control levels one week after Tau-AD inoculation (Fig. 3C). Strikingly, the loss of spines induced by photodamage, measured as the ratio of spine density after/before photodamage, was significantly reduced in both the LPS (Vehicle: 1.04 ± 0.05 vs LPS: 0.87 ± 0.04 at D2, $p = 0.029$) and Tau-AD models (Control: 1.07 ± 0.03 vs Tau-AD: 0.78 ± 0.07 at D1, $p = 0.002$; Fig. S3C), indicating a higher synapse removal activity of microglia in the neuroinflammatory contexts. Both inflammation models showed more synaptic turnover (% spines that appeared or disappeared over 2 h) after photodamage (Fig. 3C) compared to baseline (Fig. 3C; LPS model, D1: Vehicle: 17.03 ± 0.63% vs LPS: 30.25 ± 2.79%, $p = 0.0006$; LPS model, D2: Vehicle: 19.64 ± 0.97% vs LPS: 32.24 ± 1.72%, $p = 0.001$; and Tau-AD model D1: Control: 29.85 ± 2.20% vs Tau-AD: 42.57 ± 2.28%, $p = 0.007$). Within this spine turnover, spines may be lost and/or gained. However, in both LPS and Tau-AD groups, synapse elimination occurred more often than synapse formation (LPS group D2: Gained: 13.34 ± 1.30% vs Loss: 18.90 ± 1.30%, $p = 0.024$; Tau-AD, D1: Gained: 15.06 ± 1.86% vs Loss: 27.52 ± 1.74%, $p = 0.01$; Fig. 3C), which significantly increased the net spine elimination and explained the observed reduction in spine density after photodamage (Fig. S3C). One week after LPS and Tau-AD treatments, when microglia had recovered their baseline morphology

and the inoculated Aβ and Tau has been cleared (Fig. 1D, 2G), the elimination of spines also recovered to control levels.

Interestingly, we found that the spine turnover correlated with microglia contact duration (Fig. 3D) and contact area (Fig. S3C) in both inflammatory models, suggesting that microglia under pathological conditions may eliminate synapses through prolonged interactions with dendritic segments. To examine this further, we determined the distance between the site of photodamage and gained/eliminated spines (i.e., remodeling range). In both inflammation models, this remodeling range was larger than in control animals (LPS on D2 and Tau-AD on D1; Fig. S3C) and correlated with the rate of spine turnover (Fig. 3D), suggesting a loss in spatiotemporal precision of synapse removal for microglia in these animals.

To discriminate the effects of microglia interaction with synapses from the effects produced by photodamage *per se*, we introduced photodamage near imaged spines (near-spine; Fig. 4A). Similar to direct synapse ablation, photodamage near dendritic spines also resulted in a higher frequency and longer duration of microglia-dendrite contacts (Fig. 4B, S4A), and increased turnover (Tau-AD at D1: 35.55 ± 1.03% vs 42.57 ± 2.28%, $p = 0.010$; LPS at D2: 21.21 ± 2.48% vs 32.24 ± 1.72%, $p = 0.007$) (Fig. 4C) and spine loss (Tau-AD at D1: 19.22 ± 0.43 % for Near-Spine-PD vs. 27.52 ± 1.74% for Spine-PD, $p < 0.001$; LPS at D2: 12.53 ± 2.16% vs. 18.90 ± 1.30%, $p = 0.06$) (Fig. 4D, S4B) in both LPS and Tau-AD models. However, changes in turnover were less prominent than those after direct spine photodamage (Fig. S4C). Notably, photodamage near presynaptic boutons (near-bouton; Fig. 4E) also increased the contact area between microglia and axons in LPS and Tau-AD animals, but the microglia contact duration was only changed in the Tau-AD model (Fig. 4F, Fig. S5A). Surprisingly, in contrast to spines, the number of putative boutons seemed to increase after near-bouton photodamage (Fig. 4G-H, Fig. S5B), highlighting the specificity of postsynaptic versus presynaptic remodeling by microglia under inflammatory conditions.

These data indicate that photodamage-induced synaptic stress of higher and lower severity is instructive to guide microglia to areas of damage, where they may remove spines with increased efficiency under inflammatory conditions.

Since synaptic elimination by microglia was reported to involve the activation of the complement pathway, both in the context of neuroinflammation, we analyzed the correlation between these markers and parameters of synaptic remodeling (Dejanovic et al., 2018; Hong et al., 2016; Schafer et al., 2012). Notably, the observed upregulation of microglial C1q, C3R and CD68 in the inflammation models (Fig. S2A-D) correlated with spine loss (Fig. S6A) and the duration of microglia-neuron contact (Fig. S6B). To further address whether the activation of the complement pathway could be related to the enhanced synaptic remodeling, we quantified the deposition of C1q and C3 at synaptic sites. We found that the number of C1q-tagged spines increased in LPS (D2:

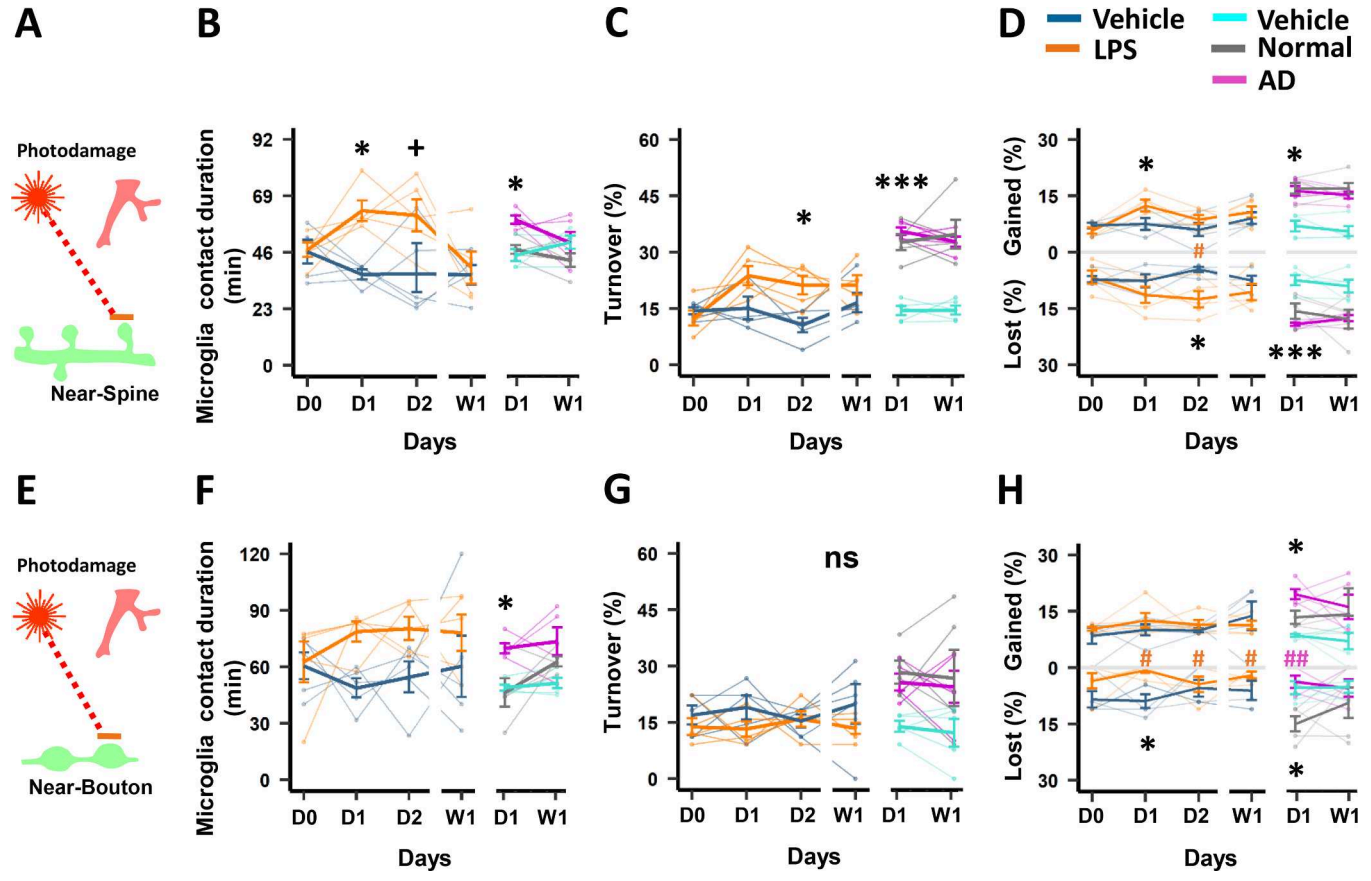

Fig. 4. Microglia-synapse interaction and synaptic remodeling following Near-Spine-PD and Near-Bouton-PD. (A-D) (A) Schematic representation of Near-Spine photodamage. (B-D) Microglia-synapse interaction and synaptic remodeling associated to Near-Spine-PD. Bold lines show group mean ± SEM values, thin lines represent individual animals (n=5 mice per group). Pink and orange hash denote significant differences between Gained % and Lost % in the LPS group at day two (D2) and the Tau-AD group at day one (D1). W1 time point is one week following the last treatment. Asterisks indicate comparisons between AD and vehicle groups and LPS and vehicle: * $p < 0.05$, ** $p < 0.01$, *** $p < 0.001$ for GEE post-hoc pairwise comparison with the Tukey method. (B-H) (E) Schematic representation of Near-Spine photodamage. (F-H) Changes in microglia-neuron interaction and synaptic remodeling parameters for Near-Bouton-PD. Pink and orange hash denote significant differences between Gained % and Lost % in the LPS group at D2 and the Tau-AD group at D1. Bold lines show group mean ± SEM values, thin lines represent individual animals (n=5 mice per group). * $p < 0.05$, ** $p < 0.01$, *** $p < 0.001$ for GEE post-hoc pairwise comparisons (AD vs. Normal and LPS vs Vehicle) with the Tukey method.

Vehicle: 19.02 ± 2.99 % vs 39.22 %, p = 0.008) and Tau-AD injected mice (D1: Normal: 17.98 ± 1.19 % vs Tau-AD: 40.31 ± 2.92 %, p = 0.0001) (Fig. 5A-B). Similarly, the number of C3-tagged spines was increased in both LPS (D1: Vehicle: 22.44 ± 3.34 % vs LPS: 56.89 ± 2.48 %, p = 0.003; D2: Vehicle: 22.44 ± 3.34 % vs 59.98 ± 2.44 %, p = 0.002) and Tau-AD (D1: Normal: 22.44 ± 3.34 % vs Tau-AD: 56.89 ± 2.48 %, p = 0.003) models (Fig. 5A-B). The percentage of spines colocalized with C1q and particularly with C3 strongly correlated with the rate of spine loss (Fig. 5A-B).

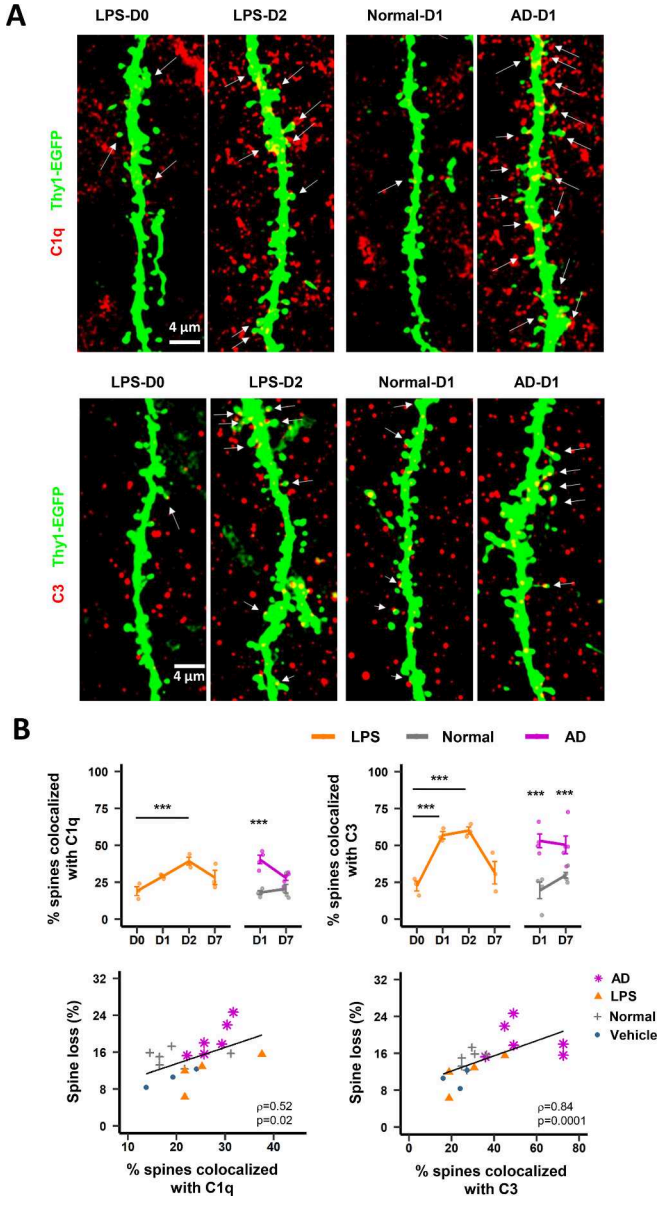

Fig. 5. Deposition of C1q and C3 on excitatory synapses. (A-B) Representative confocal images of colocalization of C1q and C3 with dendritic spines. Scale bar, 4 µm. Significantly increased number of spines tagged with C1q and C3 was observed in the RSC of mice injected with Tau-AD (day one (D1): n=4 mice in each group; week one (W1): n=5 mice in each group), but not those injected with the control extract (D1: n=4 mice in each group; W1: n=5 mice in each group). A similar effect was observed after LPS stimulation (D0, D1, D2 and W1: n=3 mice). Bold lines show group mean ± SEM values, dots represent individual animals. * $p < 0.05$, ** $p < 0.01$. GLM followed by post hoc Tukey's test. (Lower right panels) Correlations between the deposition of C1q and C3 on excitatory synapses and spine loss. Each symbol represents the mean value per animal at W1, the solid line shows linear regression. ρ, Spearman's coefficient of correlation.

In summary, our data suggest that microglia respond to pathological AD proteins and inflammation caused by LPS by activating the complement pathway, which promotes microglia-synaptic engagement via the formation of C1q-C3-C3R-mediated contacts.

3.4. Microglia induce spine elimination via induction of synaptic filopodia under inflammatory conditions

In both studied inflammatory conditions, microglia-contacted spines often carried a filopodium protruding from the head (spine-head filopodia; SHF; Fig. 6A). After spine photodamage, SHF formation was more often observed at neighboring spines in LPS and Tau-AD animals compared to respective control groups (LPS at D2: 9.32 ± 1.46% vs Control: 1.18 ± 0.01%, p = 0.008; Tau-AD at D1: 12.79 ± 1.049% vs Control: 5.19 ± 1.41%, p = 0.034; Fig. 6A, C), and had larger sizes and longer lifespans (Fig. S7A-B). Notably, the occurrence of SHFs formation significantly correlated with the duration of microglial contact (Fig. S7C) and percentage of spine loss (Fig. 6C), implicating that local microglial activity at the microglia-SHF-spine contact site may exacerbate spine elimination in the tested pathological models. Using 3D electron-microscopic reconstructions of mouse cortex (Alexander Bae et al., 2021; Shapson-Coe et al., 2021), we could confirm that microglia establish direct contacts with SHFs in normal (Fig. 6B, S7D) and inflammatory conditions (Fig. S7E). Hence, we hypothesized that microglia actively participate in the formation and elongation of the SHFs, and that formation of SHF on a spine may determine its fate.

To verify these hypotheses, we performed longitudinal imaging of individual microglia-contacted spines with SHFs. Following photodamage, 66% of SHFs involved observable microglia in their formation in the LPS-D2 group (LPS-D0: 42%) and 70% in the AD-D1 group (Normal-D1: 50%). SHF-tagged spines also had a higher probability of elimination in both pathological models (% SHF-spines eliminated by microglia: LPS at D0: 14.3% vs D2: 66.7%, p = 0.05; Tau-AD at D1: 69.23% vs Control at D1: 12.5%, p = 0.02; Fig. 6D). Specifically, via time-lapse imaging, we observed that microglia established persistent contacts with SHF and actively removed them by physically pulling them away from the dendritic branch (without visible dendritic branch alterations). During this process, the spine became encapsulated by a microglia protrusion, filopodia formation was induced at the spine head, and then the SHF-spine was pulled (stretched by approximately 5 µm in length) by the microglia. Lastly, the synapse head was internalized by microglia during microglial processes retraction (Fig. 6A; Videos S5–S7). These findings suggest that microglia use the formation of SHFs as a structural mechanism for "tagging" and elimination of spines (Fig. 6D).

To further address whether SHFs may contribute to complement opsonization of spines, we quantified the colocalization of SHFs with C1q and C3. A higher percentage of SHF colocalized with C1q in LPS (D1: Vehicle: 8.33 ± 8.33 % vs LPS: 53.66 ± 2.06, p = 0.024; D2: Vehicle: 8.33 ± 8.33 % vs LPS: 64.44 ± 2.22, p = 0.008) and Tau-AD (D1: Normal: 27.08 ± 10.42 % vs AD:74.58 ± 3.75, p = 0.009) injected mice than in control animals (Fig. 6E). Similarly, we found that SHF colocalization with C3 increased in both LPS (D2: Vehicle: 22.22 ± 2.78 % vs LPS: 62.38 ± 9.05, p = 0.020) and Tau-AD mice (D1: Normal: 25.41 ± 8.58 % vs AD:47.93 ± 2.67, p = 0.040) (Fig. 6E). In summary, our data suggest that the presence of SHF helps in the recruitment of complement molecules that may facilitate spine elimination.

Compared to control conditions, the majority of microglia-contacted spines were similarly eliminated in both inflammatory models (Fig. S8A), while less than half 'survived' without major structural changes (spine survival, pooled data for LPS and Tau-AD: 39% vs Control: 57%, p = 0.006). Furthermore, the contacted spines were more likely to be eliminated by engulfment rather than retraction (proportion of contacted spines engulfed, both with or without SHF formation: LPS and Tau-AD: 54% vs Control: 20%, p = 0.001; Fig. 7). Spines that formed filopodia were more likely to be stretched and then eliminated. Further analysis showed that the choices for spine elimination/survival, spine

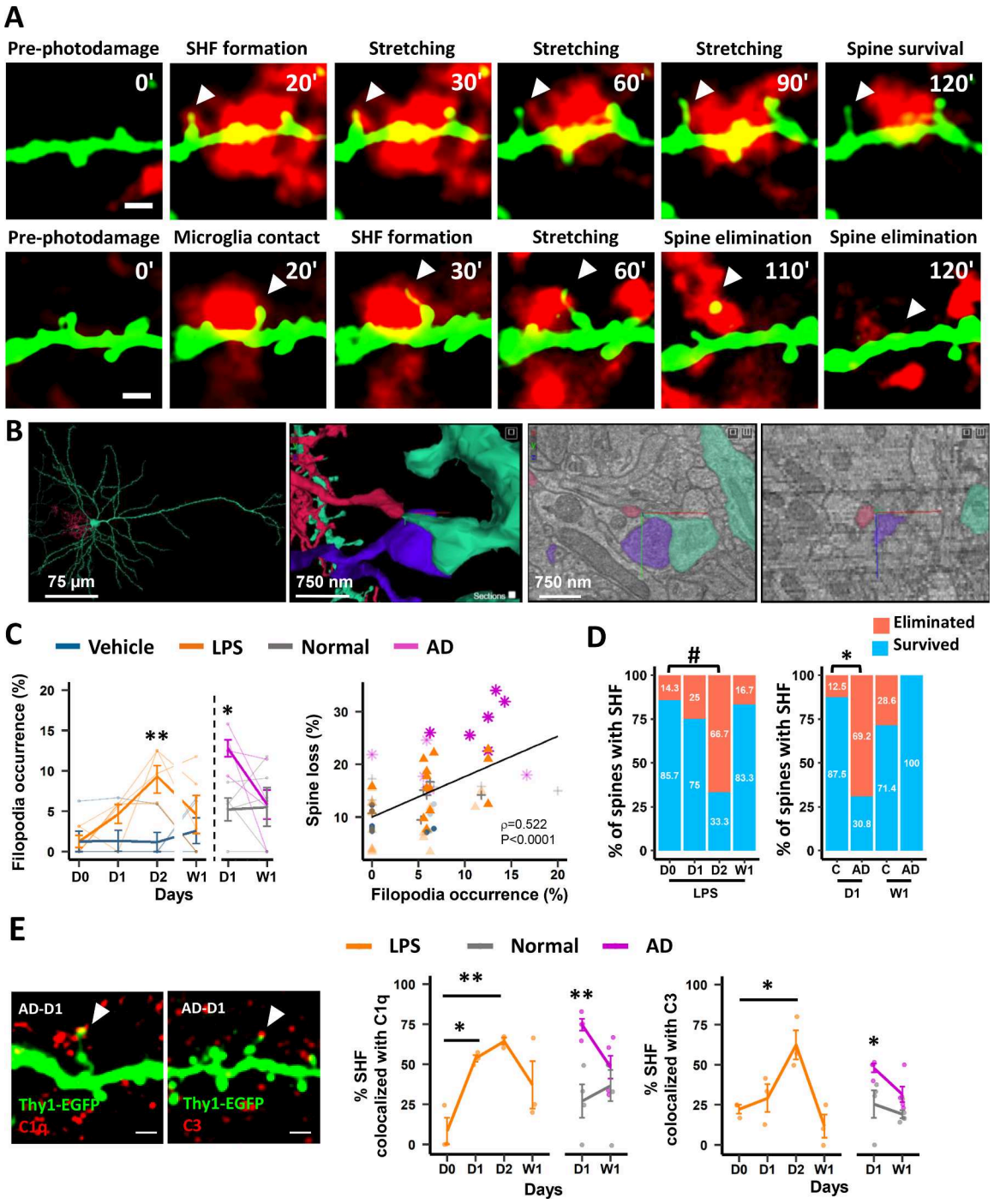

Fig. 6. Real-time mechanisms of microglia-synapse interaction and spine elimination under pathological conditions. (A) Representative images of SHF protruding from the heads of microglia-contacted spines at D1 in the Tau-AD group before (0 min) and after the photodamage. Upper panel: white head arrows show the formation of SHF, which survived until 120 min. Lower panel shows the formation of SHF from a microglia-contacted spine and its subsequent elimination via phagocytosis (white arrowhead). Scale bars, 2 µm. (B) 3D reconstruction (right) and electron microscopic images (left) showing a neuron (green) and microglia (red) and a contact between this microglial cell and SHF. 3D axes: x=red, y=green. A presynaptic terminal contacting the spine with SHF is shown in purple. Data are from a healthy young adult mouse primary visual cortex (see a link in suppl. data set 1). (C) Left, quantification of filopodia occurrence after photodamage. Asterisks show analysis of LPS vs control, and Tau-AD vs normal per day. Bold lines show group mean ± SEM values, thin lines represent individual animals (n=5 mice per group). * $p < 0.05$, ** $p < 0.01$, *** $p < 0.001$, GEE posthoc pairwise comparison with Tukey method. Right, a scatter plot shows the correlation between spine loss and filopodia occurrence. Each symbol (as in Fig. 2D) represents one photodamage experiment, the solid line shows linear regression. ρ, Spearman coefficient of correlation. (D) Quantification of the percentage of spines that were eliminated or survived after the formation of SHF in the LPS and Tau-AD groups. Statistical comparisons were performed using the Fisher's exact test (#: p-value=0.05, * $p < 0.05$). (E) Deposition of C1q and C3 on SHF. White arrows denote SHFs. Scale bar, 2 µm. Significantly increased number of SHF tagged with C1q and C3 was observed in the RSC of mice injected with Tau-AD on day one (D1): n=4 mice in each group; week one (W1): n=5 mice in each group), but not those injected with the control extract (D1: n=4 mice in each group; W1: n=5 mice in each group). A similar effect was observed after LPS stimulation (D0, D1, D2 and W1: n=3 mice). Bold lines show group mean ± SEM values, dots represent individual animals. * $p < 0.05$, ** $p < 0.01$. GLM followed by post hoc Tukey's test.

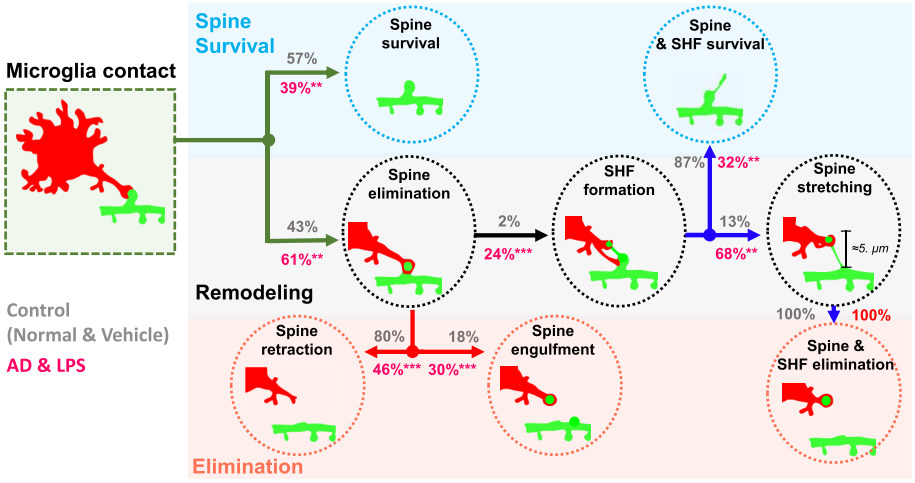

Fig. 7. Schematic representation of the putative events of synaptic remodeling by microglia during systemic inflammation and tauopathy. Photodamage induces a contact of microglia with some spines. This contact can be rapid and the spine survives or it becomes prolonged and then the spine can be eliminated by retraction of the spine, or by engulfment with or without SHF formation. Engulfment with SHF involves apparent stretching and pulling out of the spine from the dendritic shaft by microglia. Percentages indicate the transition rates for pathological conditions (LPS + AD, pink) and controls (Vehicle + Normal, grey). ** $p < 0.01$, *** $p < 0.001$, Fisher's exact test. Green, red and blue arrows show the choices for spine elimination/survival or engulfment/retraction or SHF elimination/survival, respectively.

engulfment/retraction, and SHF elimination/survival were highly dependent on the microglia contact duration and distance from the photodamage site, and did not depend on the size or lifetime of the SHF (Fig. S8B). These results indicate that microglia similarly eliminate spines under two studied pathological conditions in three different ways: spine retraction (52% in LPS and 39% in Tau-AD), phagocytosis (28% in LPS and 32% in Tau-AD) and via the formation of SHFs (SHF: 21% in LPS and 29% in Tau-AD; Fig. S8A, 7).

4. Discussion

In this study we used longitudinal *in vivo* two-photon imaging to observe microglia-neuron interactions in two acute models of inflammation, systemic treatment with LPS or focal inoculation of insoluble aggregated proteins from human AD brain. In both models, inflammation resulted in i) reduced frequency of microglia surveillance contacts of dendritic spines; ii) longer duration of microglial contacts after synaptic stress induced by photodamage of single synaptic sites; iii) increased synaptic turnover and spine loss; and iv) a changed mode of spine elimination, involving more frequently the formation of spine head filopodia followed by spine phagocytosis.

LPS and Tau-AD treatment decreased the contact frequency of microglia with spines by prolonging the contact with fewer spines, indicating that microglia had an impaired rate of basal surveillance under these two conditions. This observation is in line with previous studies in ischemia models, traumatic brain injury and after repetitive systemic injections of LPS (Chen et al., 2014; Krukowski et al., 2021; Wake et al., 2009; Akiyoshi et al., 2018). Controlled synaptic stress by photodamage at or next to individual synapses attracted microglia processes to dendrites and axons in the area around the damage and increased the probability for synapses to be remodeled or eliminated. The position of the photodamage on (direct damage/stress) or nearby (indirect stress) the imaged neural structures determined different levels of damage and synaptic stress severity for the imaged dendrite. Both types of photodamage enhanced the recruitment of microglial processes to the area around the damage and promoted synaptic elimination in inflammatory conditions. Previously, microglial activity in synapse remodeling was indirectly estimated to be enhanced in other animal models of synaptic stress/damage, such as ischemia (Wake et al., 2009), systemic inflammation (Chen et al., 2014; Gallo et al., 2022), stress (Liu et al., 2021) and AD (Gervais et al., 2021; Gratuze et al., 2021; Wright et al., 2013), which together with our present data validates the use of synaptic photodamage as a model of synaptic stress to study microglia-neuron interactions. Together, these studies and our current results support the hypothesis that early inflammatory changes occurring in different diseases, including AD and systemic inflammation, may facilitate synaptic elimination by microglia.

Interestingly, the two inflammatory stimuli used in this study may activate different pathways that converge on a common regulation of microglial phagocytic activity towards spines independently of the route of administration (intraperitoneal/intracerebral). As shown by proteomics studies of isolated microglia cells, the difference between these two models is that while LPS-treatment induced proliferative responses, AD pathology inhibited cell proliferation and promotes apoptosis (upregulation of proteins such as p53 and AP2) despite the similarities in general upregulation of pro-inflammatory proteins (Clu, Nudt2, Glipr2, Diablo and Cstf2) and common IL4-related pathways (Rangaraju et al., 2018). As the upstream transcriptional regulators of AD-associated microglial activation (p53, AP-2 and PUR2α) are distinct from those of canonical LPS-induced pro-inflammatory activation (TLR4/NF-kappaB signaling) (Rangaraju et al., 2018), it suggests that AD-associated microglial activation uses unique apoptotic pathways to remodel synapses compared to LPS, resulting in higher levels of spine remodeling and elimination.

The observed synaptic remodeling in our experiments may lead to impairments in neural activity and cognitive processing reported in these two models. Previously it has been shown that LPS (Maggio et al., 2013; Shemer et al., 2020; Strehl et al., 2014), human AD brain-derived tau oligomers (Lasagna-Reeves et al., 2012) and amyloid-beta oligomers (Hong et al., 2016) acutely injected into wild-type mice impair LTP in the hippocampal area. Moreover, social withdrawal and depressive-like behavior (Dantzer et al., 2008; Duan et al., 2018; Henry et al., 2008; Kreisel et al., 2014), appetite loss (Kreisel et al., 2014; Jiang et al., 2022), reduced motility and exploratory activity (Shemer et al., 2020; Kreisel et al., 2014), reduced spatial memory in the Morris water maze test (Lee et al., 2008; Noh et al., 2014; Schreuder et al., 2017; Zhao et al., 2019) and failure in the object recognition test (Lasagna-Reeves et al., 2012, Lam et al., 2022) have been reported following microglial activation. The acute changes in microglia-synapse interactions observed after one and two days following LPS injection may also impact neuronal circuit function. According to a previous study, when microglia are activated with consecutive low doses of LPS, their frequency of contact with synapses decreases (as we also observed in the present study), resulting in a reduction in the synchronized firing of neurons (Akiyoshi et al., 2018). Changes may disappear over time (weeks) depending on the LPS dose and the number of injections, but long-term changes may still occur as previous studies have demonstrated decreased spine density over months of a single dose of LPS (Kondo et al., 2011). In this study, we further showed that synaptic engulfment by microglia is enhanced and their ability to modify and remove synapses is exacerbated. This synaptic remodeling is likely to contribute to the previously reported changes in neural circuit synchronization, synaptic plasticity,

and behavior related to inflammation.

Under normal conditions, microglia are attracted via ATP/ADP-dependent mechanisms to active synaptic sites and may promote synapse formation and support Hebbian synaptic plasticity, e.g. via BDNF release. However, under inflammatory conditions we observed that the attraction of microglia results in a preferential loss of synapses, which would prohibit rather than support Hebbian plasticity and impair the acquisition of spatial memories (Lee et al., 2008; Noh et al., 2014; Schreuder et al., 2017; Zhao et al., 2019) and also lead to forgetting (Wang et al., 2020). Additionally, our study demonstrates general exacerbation of synaptic remodeling with a strong increase in both spine formation and spine elimination in both neuroinflammatory models used. This may compromise existing memories due to the formation of new erroneous synaptic connections, resulting, for instance, in impaired discrimination of objects (Lasagna-Reeves et al., 2012, Lam et al., 2022). In relation to this, our current study found that a postsynaptic spine loss was accompanied by increased generation of presynaptic boutons during neuroinflammation. This suggests that there could be an increase in the number of complex synapses with multiple presynaptic innervations, which may facilitate integration of information at the expense of object/context discrimination.

Using the focal synaptic photodamage approach, we were able to reveal new mechanisms of how microglia remove spines in the living brain. Our data show that microglia induce SHFs on (selected) contacted spines and physically pull them away from the dendritic branch through microglial process retraction. This leads to a stretching and eventually removal of the SHF-synapse. The observation that microglia can remove specific parts of neurons is consistent with a previous report, in which phagocytic microglia contacted apoptotic dendrites with their processes and, 6 h later, had neuronal inclusions in the respective processes (Damisah et al., 2020). Similarly, macrophage branches have been reported to elongate, retract, and physically pull particles towards them or pinch off membrane fragments from other cells (Kress et al., 2007; Morini et al., 2021). These processes have also more recently been referred to as trogocytosis (e.g., see Bettadapur et al., 2020).

The differential strategies of microglia in synaptic elimination may depend on the duration and degree of synaptic damage. If the damage is at an advanced stage, multiple mechanisms such as accumulation of calcium, activation of caspases, secretion of extracellular proteases, exposure of phosphatidylserine and C1 deposition in spines may be activated (Györffy et al., 2018; Nonaka and Nakanishi, 2019). These mechanisms may also affect the size and strength of adhesive contacts between individual spines and astroglial processes as well as the spine coverage by perisynaptic extracellular matrix. Depending on its composition, the latter may serve as a barrier for microglia invasion and spine engulfment (Nguyen et al., 2020) or be tagged by complement proteins and promote microglial contact. The removal of astroglial and extracellular matrix barriers would allow microglia to directly contact and eliminate spines. In the case of mild synaptic damage and/or better preserved “barriers”, intermediate steps such as formation of filopodia may be required.

Microglia were previously shown to contribute to the formation of SHFs during normal conditions (Cangalaya et al., 2020) and early developmental stages (Miyamoto et al., 2016; Weinhard et al., 2018), and SHFs have been related to synapse formation or spine relocation in vitro (Weinhard et al., 2018) and in response to altered neuronal activity (Richards et al., 2005; Szepesi et al., 2013) or learning (Nguyen et al., 2020). Here, however, we observed an increase in SHFs in neuroinflammatory conditions and in correlation with spine loss, which highlights a new role of SHFs. Moreover, the formation of SHFs could not only result in a reduction of spine numbers, but also in a reduction of spine head size, which has previously been linked to cognitive dysfunction in AD (Boros et al., 2019). The survival of SHF may also be linked to the formation of multi-innervated spines. In our study, we minimized laser irradiation and had a limited (10-min) temporal resolution, but this temporal resolution is well within the duration of microglia-synapse contact under inflammatory conditions. Still, we cannot exclude that there are additional intermediate events taking place between the formation of spine head filopodia and the elimination of spines, including trogocytosis (Weinhard et al., 2018), which may warrant further investigation using even higher temporal and spatial resolution.

A possible mechanism underlying the enhanced microglial synaptic remodeling that we observed in inflammatory conditions may be the activation of the complement pathway. Elevated C1q, C3, and C3R expression at the photodamage area correlated with spine loss in both tested inflammation models. Moreover, we found increased colocalization of these proteins with spines. While it is still unclear which specific complement receptors are present at synapses, studies have shown that these proteins can attached directly to synaptosomes and their deposition at synaptic sites may be trigger by Aβ, tau protein, and/or large amounts of proinflammatory cytokines (Xin et al., 2019). Complement proteins may accumulate at spines and thereby increase the probability of their phagocytosis by microglia through the formation of C3R-C3-C1q complexes (Hong et al., 2016). In addition, we found that SHF were C1q and C3 immunopositive, suggesting that these structures may participate in the removal of the spine by microglia mediation via the activation of the complement pathway. However, further studies are needed to verify a causal link between the complement system and the different modes of spine remodeling we observed, particularly those involving the formation of SHFs in inflammatory conditions. In summary, our findings reveal novel cellular mechanisms of microglial synaptic remodeling in the context of Alzheimer’s disease and systemic inflammation. These findings may provide valuable insight towards the development of therapeutic interventions for preventing microglia-related synapse loss in these conditions.

Declaration of Competing Interest

The authors declare that they have no known competing financial interests or personal relationships that could have appeared to influence the work reported in this paper.

Data availability

Data will be made available on request.

Acknowledgements

The project has been supported by the federal state Saxony-Anhalt and the European Structural and Investment Funds (ESF), project number ZS/2016/08/80645 (to KDF and AD), Deutsche Forschungsgemeinschaft (DFG, German Research Foundation) – 362321501/RTG 2413 SynAGE (to AD), and the European Regional Development Fund (ERDF: Center for Behavioral Brain Sciences ZS/2016/04/78113 to JP). We thank Dr. Anne Maass for her critical comments on the manuscript.

Appendix A. Supplementary data

Supplementary data to this article can be found online at https://doi.org/10.1016/j.bbi.2023.02.023.

References

Akiyoshi, R., Wake, H., Kato, D., horiuchi, H., Ono, R., Ikegami, A., Haruwaka, K., Omori, T., Tachibana, Y., Moorhouse, A.J., Nabekura, J., 2018. Microglia Enhance Synapse Activity to Promote Local Network Synchronization. eNeuro 5, ENEURO.0088-0018.2018.

Alexander Bae, J., Baptiste, M., Bodor, A.L., Brittain, D., Buchanan, J., Bumbarger, D.J., Castro, M.A., Celii, B., Cobos, E., Collman, F., da Costa, N.M., Dorkenwald, S., Elabbady, L., Fahey, P.G., Fliss, T., Froudakis, E., Gager, J., Gamlin, C., Halageri, A., Hebditch, J., Jia, Z., Jordan, C., Kapner, D., Kemnitz, N., Kinn, S., Koolman, S., Kuehner, K., Lee, K., Li, K., Lu, R., Macrina, T., Mahalingam, G., McReynolds, S.,

Miranda, E., Mitchell, E., Mondal, S.S., Moore, M., Mu, S., Muhammad, T., Nehoran, B., Ogedengbe, O., Papadopoulos, C., Papadopoulos, S., Patel, S., Pitkow, X., Popovych, S., Ramos, A., Clay Reid, R., Reimer, J., Schneider-Mizell, C.M., Sebastian Seung, H., Silverman, B., Silversmith, W., Sterling, A., Sinz, F.H., Smith, C.L., Suckow, S., Tan, Z.H., Tolias, A.S., Torres, R., Turner, N.L., Walker, E.Y., Wang, T., Williams, G., Williams, S., Willie, K., Willie, R., Wong, W., Wu, J., Xu, C., Yang, R., Yatsenko, D., Ye, F., Yin, W., Yu, S.-c., 2021. Functional connectomics spanning multiple areas of mouse visual cortex. bioRxiv, 2021.2007.2028.454025.

Andersson, P.B., Perry, V.H., Gordon, S., 1992. The acute inflammatory response to lipopolysaccharide in CNS parenchyma differs from that in other body tissues. Neuroscience 48, 169–186.

Arganda-Carreras, I., Fernández-González, R., Muñoz-Barrutia, A., Ortiz-De-Solorzano, C., 2010 Oct. 3D reconstruction of histological sections: Application to mammary gland tissue. Microsc Res Tech 73 (11), 1019–1029.

Bettadapur, A., Miller, H.W., Ralston, K.S., 2020 Jun 22. Biting Off What Can Be Chewed: Trogocytosis in Health, Infection, and Disease. Infect Immun. 88 (7), e00930–e01019.

Bolós, M., Llorens-Martín, M., Jurado-Arjona, J., Hernández, F., Rábano, A., Avila, J., 2016. Direct Evidence of Internalization of Tau by Microglia In Vitro and In Vivo. J. Alzheimer's Dis. JAD 50, 77–87.

Boros, B.D., Greathouse, K.M., Gearing, M., Herskowitz, J.H., 2019. Dendritic spine remodeling accompanies Alzheimer's disease pathology and genetic susceptibility in cognitively normal aging. Neurobiol. Aging 73, 92–103.

Cai, Q., Tammineni, P., 2017. Mitochondrial Aspects of Synaptic Dysfunction in Alzheimer's Disease. J. Alzheimer's Dis. JAD 57, 1087–1103.

Cangalaya, C., Stoyanov, S., Fischer, K.D., Dityatev, A., 2020. Light-induced engagement of microglia to focally remodel synapses in the adult brain. Elife 9, e58435.

Chen, Z., Jalabi, W., Hu, W., Park, H.J., Gale, J.T., Kidd, G.J., Bernatowicz, R., Gossman, Z.C., Chen, J.T., Dutta, R., Trapp, B.D., 2014. Microglial displacement of inhibitory synapses provides neuroprotection in the adult brain. Nat. Commun. 5, 4486.

D'Amelio, M., Cavallucci, V., Middei, S., Marchetti, C., Pacioni, S., Ferri, A., Diamantini, A., De Zio, D., Carrara, P., Battistini, L., Moreno, S., Bacci, A., Ammassari-Teule, M., Marie, H., Cecconi, F., 2011. Caspase-3 triggers early synaptic dysfunction in a mouse model of Alzheimer's disease. Nat. Neurosci. 14, 69–76.

Damisah, E.C., Hill, R.A., Rai, A., Chen, F., Rothlin, C.V., Ghosh, S., Grutzendler, J., 2020. Astrocytes and microglia play orchestrated roles and respect phagocytic territories during neuronal corpse removal in vivo. Sci. Adv. 6, eaba3239.

Dantzer, R., O'Connor, J.C., Freund, G.G., Johnson, R.W., Kelley, K.W., 2008 Jan. From inflammation to sickness and depression: when the immune system subjugates the brain. Nat. Rev. Neurosci. 9 (1), 46–56.

Dejanovic, B., Huntley, M.A., De Mazière, A., Meilandt, W.J., Wu, T., Srinivasan, K., Jiang, Z., Gandham, V., Friedman, B.A., Ngu, H., Foreman, O., Carano, R.A.D., Chih, B., Klumperman, J., Bakalarski, C., Hanson, J.E., Sheng, M., 2018. Changes in the Synaptic Proteome in Tauopathy and Rescue of Tau-Induced Synapse Loss by C1q Antibodies. Acta Neuropathol. Commun. 100, 1322–1336.e1327.

Devi, L., Prabhu, B.M., Galati, D.F., Avadhani, N.G., Anandatheerthavarada, H.K., 2006. Accumulation of amyloid precursor protein in the mitochondrial import channels of human Alzheimer's disease brain is associated with mitochondrial dysfunction. Nat. Commun. 26, 9057–9068.

Duan, L., Zhang, X.D., Miao, W.Y., Sun, Y.J., Xiong, G., Wu, Q., Li, G., Yang, P., Yu, H., Li, H., Wang, Y., Zhang, M., Hu, L.Y., Tong, X., Zhou, W.H., Yu, X., 2018 Oct 10. PDGFRβ Cells Rapidly Relay Inflammatory Signal from the Circulatory System to Neurons via Chemokine CCL2. Neuron 100 (1), 183–200.e8.

Dzyubenko, E., Rozenberg, A., Hermann, D.M., Faissner, A., 2016 Nov. Colocalization of synapse marker proteins evaluated by STED-microscopy reveals patterns of neuronal synapse distribution in vitro. J. Neurosci. Methods. 1 (273), 149–159.

Feng, G, Mellor, RH, Bernstein, M, Keller-Peck, C, Nguyen, QT, Wallace, M, Nerbonne, JM, Lichtman, JW, Sanes, JR, 2000 Oct. Imaging neuronal subsets in transgenic mice expressing multiple spectral variants of GFP. Neuron 28 (1), 41–51.

Fernández-Arjona, M.D.M., Grondona, J.M., Fernández-Llebrez, P., López-Ávalos, M.D., 2019. Microglial Morphometric Parameters Correlate With the Expression Level of IL-1β, and Allow Identifying Different Activated Morphotypes. Front. Cell. Neurosci. 13, 472.

Gallo, N.B., Berisha, A., Van Aelst, L., 2022. Microglia regulate chandelier cell axo-axonic synaptogenesis. Proc. Natl. Acad. Sci. USA 119, e2114.

Gervais, É., Iloun, P., Martianova, E., Gonçalves Bessa, A.C., Rivest, S., Topolnik, L., 2021. Structural analysis of the microglia-interneuron interactions in the CA1 hippocampal area of the APP/PS1 mouse model of Alzheimer's disease. J. Comp. Neurol. 530, 1423–1437.

Gratuze, M., Chen, Y., Parhizkar, S., Jain, N., Strickland, M.R., Serrano, J.R., colonna, M., Ulrich, J.D., Holtzman, D.M.,, 2021. Activated microglia mitigate Aβ-associated tau seeding and spreading. J. Exp. Med. 218, e20210542.

Györffy, B.A., Kun, J., Török, G., Bulyáki, É., Borhegyi, Z., Gulyássy, P., Kis, V., Szocsics, P., Micsonai, A., Matkó, J., Drahos, L., Juhász, G., Kékesi, K.A., Kardos, J., 2018 Jun 12. Local apoptotic-like mechanisms underlie complement-mediated synaptic pruning. Proc. Natl. Acad. Sci. U S A 115 (24), 6303–6308.

Hammond, T.R., Dufort, C., Dissing-Olesen, L., Giera, S., Young, A., Wysoker, A., Walker, A.J., Gergits, F., Segel, M., Nemesh, J., Marsh, S.E., Saunders, A., Macosko, E., Ginhoux, F., Chen, J., Franklin, R.J.M., Piao, X., McCarroll, S.A., Stevens, B., 2019. Single-Cell RNA Sequencing of Microglia throughout the Mouse Lifespan and in the Injured Brain Reveals Complex Cell-State Changes. Immunity 50, 253–271.e256.

Haynes, S.E., Hollopeter, G., Yang, G., Kurpius, D., Dailey, M.E., Gan, W.B., Julius, D., 2006. The P2Y12 receptor regulates microglial activation by extracellular nucleotides. Nat. Neurosci. 9, 1512–1519.

He, X.F., Xu, J.H., Li, G., Li, M.Y., Li, L.L., Pei, Z., Zhang, L.Y., Hu, X.Q., 2020. NLRP3-dependent microglial training impaired the clearance of amyloid-beta and aggravated the cognitive decline in Alzheimer's disease. Cell Death Dis. 11, 849.

Henry, C.J., Huang, Y., Wynne, A., Hanke, M., Himler, J., Bailey, M.T., Sheridan, J.F., Godbout, J.P., 2008 May. Minocycline attenuates lipopolysaccharide (LPS)-induced neuroinflammation, sickness behavior, and anhedonia. J Neuroinflammation. 13 (5), 15.

Holtmaat, A.J., Trachtenberg, J.T., Wilbrecht, L., Shepherd, G.M., Zhang, X., Knott, G.W., Svoboda, K., 2005 Jan 20. Transient and persistent dendritic spines in the neocortex in vivo. Neuron 45 (2), 279–291.

Hong, S., Beja-Glasser, V.F., Nfonoyim, B.M., Frouin, A., Li, S., Ramakrishnan, S., Merry, K.M., Shi, Q., Rosenthal, A., Barres, B.A., Lemere, C.A., Selkoe, D.J., Stevens, B., 2016. Complement and microglia mediate early synapse loss in Alzheimer mouse models. Science 352, 712–716.

Jiang, J., Tang, B., Wang, L., Huo, Q., Tan, S., Misrani, A., Han, Y., Li, H., Hu, H., Wang, J., Cheng, T., Tabassum, S., Chen, M., Xie, W., Long, C., Yang, L., 2022 Jan. Systemic LPS-induced microglial activation results in increased GABAergic tone: A mechanism of protection against neuroinflammation in the medial prefrontal cortex in mice. Brain Behav. Immun. 99, 53–69.

Keller, J.N., Lauderback, C.M., Butterfield, D.A., Kindy, M.S., Yu, J., Markesbery, W.R., 2000. Amyloid beta-peptide effects on synaptosomes from apolipoprotein E-deficient mice. J. Neurochem. 74, 1579–1586.

Kettenmann, H., Hanisch, U.K., Noda, M., Verkhratsky, A., 2011. Physiology of microglia. Physiol. Rev. 91, 461–553.

Kettenmann, H., Kirchhoff, F., Verkhratsky, A., 2013. Microglia: new roles for the synaptic stripper. Neuron 77, 10–18.

Kondo, S., Kohsaka, S., Okabe, S., 2011. Long-term changes of spine dynamics and microglia after transient peripheral immune response triggered by LPS in vivo. Mol. Brain 4, 27.

Kreisel, T., Frank, M.G., Licht, T., Reshef, R., Ben-Menachem-Zidon, O., Baratta, M.V., Maier, S.F., Yirmiya, R., 2014 Jun. Dynamic microglial alterations underlie stress-induced depressive-like behavior and suppressed neurogenesis. Mol Psychiatry 19 (6), 699–709.

Kress, H., Stelzer, E.H., Holzer, D., Buss, F., Griffiths, G., Rohrbach, A., 2007. Filopodia act as phagocytic tentacles and pull with discrete steps and a load-dependent velocity. Proc. Natl. Acad. Sci. USA 104, 11633–11638.

Krukowski, K., Nolan, A., Becker, M., Picard, K., Vernoux, N., Frias, E.S., Feng, X., Tremblay, M.E., Rosi, S., 2021. Novel microglia-mediated mechanisms underlying synaptic loss and cognitive impairment after traumatic brain injury. Brain Behav. Immun. 98, 122–135.

Lam, S., Hérard, A.S., Boluda, S., Petit, F., Eddarkaoui, S., Cambon, K., Picq, J.L., Buée, L., Duyckaerts, C., Haïk, S., Dhenain, M., 2022. Pathological changes induced by Alzheimer's brain inoculation in amyloid-beta plaque-bearing mice. Acta Neuropathol. Commun. 10, 112.

Lasagna-Reeves, C.A., Castillo-Carranza, D.L., Sengupta, U., Guerrero-Munoz, M.J., Kiritoshi, T., Neugebauer, V., Jackson, G.R., Kayed, R., 2012. Alzheimer brain-derived tau oligomers propagate pathology from endogenous tau. Sci. Rep. 2, 700.

Lee, J.W., Lee, Y.K., Yuk, D.Y., Choi, D.Y., Ban, S.B., Oh, K.W., Hong, J.T., 2008. Neuro-inflammation induced by lipopolysaccharide causes cognitive impairment through enhancement of beta-amyloid generation. J. Neuroinflammation 5, 37.

Li, S.M., Li, B., Zhang, L., Zhang, G.F., Sun, J., Ji, M.H., Yang, J.J., 2020. A complement-microglial axis driving inhibitory synapse related protein loss might contribute to systemic inflammation-induced cognitive impairment. Int. Immunopharmacol. 87, 106814.

Liu, T., Lu, J., Lukasiewicz, K., Pan, B., Zuo, Y., 2021. Stress induces microglia-associated synaptic circuit alterations in the dorsomedial prefrontal cortex. Neurobiol. Stress 15, 100342.

Luo, W., Liu, W., Hu, X., Hanna, M., Caravaca, A., Paul, S.M., 2015. Microglial internalization and degradation of pathological tau is enhanced by an anti-tau monoclonal antibody. Sci. Rep. 5, 11161.

Madisen, L., Zwingman, T.A., Sunkin, S.M., Oh, S.W., Zariwala, H.A., Gu, H., Ng, L.L., Palmiter, R.D., Hawrylycz, M.J., Jones, A.R., Lein, E.S., Zeng, H., 2010 Jan. A robust and high-throughput Cre reporting and characterization system for the whole mouse brain. Nat Neurosci 13 (1), 133–140.

Maggio, N., Shavit-Stein, E., Dori, A., Blatt, I., Chapman, J., 2013 Dec. Prolonged systemic inflammation persistently modifies synaptic plasticity in the hippocampus: modulation by the stress hormones. Front. Mol. Neurosci. 4 (6), 46.

Majumdar, A., Cruz, D., Asamoah, N., Buxbaum, A., Sohar, I., Lobel, P., Maxfield, F.R., 2007 Apr. Activation of microglia acidifies lysosomes and leads to degradation of Alzheimer amyloid fibrils. Mol. Biol. Cell. 18 (4), 1490–1496.

Manabe, T., Rácz, I., Schwartz, S., Oberle, L., Santarelli, F., Emmrich, J.V., Neher, J.J., Heneka, M.T., 2021. Systemic inflammation induced the delayed reduction of excitatory synapses in the CA3 during ageing. J. Neurochem. 159, 525–542.

Meyer-Luehmann, M., Spires-Jones, T.L., Prada, C., Garcia-Alloza, M., de Calignon, A., Rozkalne, A., Koenigsknecht-Talboo, J., Holtzman, D.M., Bacskai, B.J., Hyman, B.T., 2008. Rapid appearance and local toxicity of amyloid-beta plaques in a mouse model of Alzheimer's disease. Nature 451, 720–724.

Miyamoto, A., Wake, H., Ishikawa, A.W., Eto, K., Shibata, K., Murakoshi, H., Koizumi, S., 2016. Microglia contact induces synapse formation in developing somatosensory cortex. Nat. Commun. 7, 12540.

Morini, R., Bizzotto, M., Perrucci, F., Filipello, F., Matteoli, M., 2021. Strategies and Tools for Studying Microglial-Mediated Synapse Elimination and Refinement. Nat. Commun. 12, 640937.

Nguyen, P.T., Dorman, L.C., Pan, S., Vainchtein, I.D., Han, R.T., Nakao-Inoue, H., Taloma, S.E., Barron, J.J., Molofsky, A.B., Kheirbek, M.A., Molofsky, A.V., 2020.

Microglial Remodeling of the Extracellular Matrix Promotes Synapse Plasticity. Cell 182, 388–403.e315.
Noh, H., Jeon, J., Seo, H., 2014. Systemic injection of LPS induces region-specific neuroinflammation and mitochondrial dysfunction in normal mouse brain. Neurochem. Int. 69, 35–40.
Nonaka, S., Nakanishi, H., 2019. Microglial clearance of focal apoptotic synapses. Neurosci. Lett. 707, 134317.
Patterson, G.H., Knobel, S.M., Sharif, W.D., Kain, S.R., Piston, D.W., 1997 Nov. Use of the green fluorescent protein and its mutants in quantitative fluorescence microscopy. Biophys J. 73 (5), 2782–2790.
Pickett, E.K., Herrmann, A.G., McQueen, J., Abt, K., Dando, O., Tulloch, J., Jain, P., Dunnett, S., Sohrabi, S., Fjeldstad, M.P., Calkin, W., Murison, L., Jackson, R.J., Tzioras, M., Stevenson, A., d'Orange, M., Hooley, M., Davies, C., Colom-Cadena, M., Anton-Fernandez, A., King, D., Oren, I., Rose, J., McKenzie, C.A., Allison, E., Smith, C., Hardt, O., Henstridge, C.M., Hardingham, G.E., Spires-Jones, T.L., 2019. Amyloid Beta and Tau Cooperate to Cause Reversible Behavioral and Transcriptional Deficits in a Model of Alzheimer's Disease. Cell Rep. 29, 3592–3604.e3595.
Rangaraju, S., Dammer, E.B., Raza, S.A., Gao, T., Xiao, H., Betarbet, R., Duong, D.M., Webster, J.A., Hales, C.M., Lah, J.J., Levey, A.I., Seyfried, N.T., 2018 Jun 28. Quantitative proteomics of acutely-isolated mouse microglia identifies novel immune Alzheimer's disease-related proteins. Mol. Neurodegener. 13 (1), 34.
Reddy, P.H., Beal, M.F., 2008. Amyloid beta, mitochondrial dysfunction and synaptic damage: implications for cognitive decline in aging and Alzheimer's disease. Trends Mol. Med. 14, 45–53.
Richards, D.A., Mateos, J.M., Hugel, S., de Paola, V., Caroni, P., Gähwiler, B.H., McKinney, R.A., 2005. Glutamate induces the rapid formation of spine head protrusions in hippocampal slice cultures. Proc. Natl. Acad. Sci. USA 102, 6166–6171.
Salter, M.W., Stevens, B., 2017. Microglia emerge as central players in brain disease. Proc. Natl. Acad. Sci. USA 23, 1018–1027.
Savage, J.C., St-Pierre, M.K., Hui, C.W., Tremblay, M.E., 2019. Microglial Ultrastructure in the Hippocampus of a Lipopolysaccharide-Induced Sickness Mouse Model. eLife 13, 1340.
Schafer, D.P., Lehrman, E.K., Kautzman, A.G., Koyama, R., Mardinly, A.R., Yamasaki, R., Ransohoff, R.M., Greenberg, M.E., Barres, B.A., Stevens, B., 2012. Microglia sculpt postnatal neural circuits in an activity and complement-dependent manner. Neuron 74, 691–705.
Schafer, D.P., Lehrman, E.K., Heller, C.T., Stevens, B., 2014 Jun 8. An engulfment assay: a protocol to assess interactions between CNS phagocytes and neurons. J. Vis. Exp. 88, 51482.
Schreuder, L., Eggen, B.J., Biber, K., Schoemaker, R.G., Laman, J.D., de Rooij, S.E., 2017. Pathophysiological and behavioral effects of systemic inflammation in aged and diseased rodents with relevance to delirium: A systematic review. Brain Behav. Immun. 62, 362–381.
Shapson-Coe, A., Januszewski, M., Berger, D.R., Pope, A., Wu, Y., Blakely, T., Schalek, R. L., Li, P.H., Wang, S., Maitin-Shepard, J., Karlupia, N., Dorkenwald, S., Sjostedt, E., Leavitt, L., Lee, D., Bailey, L., Fitzmaurice, A., Kar, R., Field, B., Wu, H., Wagner-Carena, J., Aley, D., Lau, J., Lin, Z., Wei, D., Pfister, H., Peleg, A., Jain, V., Lichtman, J.W., 2021. A connectomic study of a petascale fragment of human cerebral cortex. bioRxiv, 2021.2005.2029.446289.
Shemer, A., Scheyltjens, I., Frumer, G.R., Kim, J.S., Grozovski, J., Ayanaw, S., Dassa, B., Van Hove, H., Chappell-Maor, L., Boura-Halfon, S., Leshkowitz, D., Mueller, W., Maggio, N., Movahedi, K., Jung, S., 2020 Nov 17. Interleukin-10 Prevents Pathological Microglia Hyperactivation following Peripheral Endotoxin Challenge. Immunity 53 (5), 1033–1049.e7.
Stoyanov, S., Sun, W., Düsedau, H.P., Cangalaya, C., Choi, I., Mirzapourdelavar, H., Baidoe-Ansah, D., Kaushik, R., Neumann, J, Dunay, I.R., Dityatev, A., 2021 Jan. Attenuation of the extracellular matrix restores microglial activity during the early stage of amyloidosis. Glia 69 (1), 182–200.
Strehl, A., Lenz, M., Itsekson-Hayosh, Z., Becker, D., Chapman, J., Deller, T., Maggio, N., Vlachos, A., 2014 Nov. Systemic inflammation is associated with a reduction in Synaptopodin expression in the mouse hippocampus. Exp. Neurol. 261, 230–235.
Streit, W.J., Mrak, R.E., Griffin, W.S., 2004. Microglia and neuroinflammation: a pathological perspective. J. Neuroinflammation 1, 14.
Sun, W., Suzuki, K., Toptunov, D., Stoyanov, S., Yuzaki, M., Khiroug, L., Dityatev, A., 2019. *In vivo* Two-Photon Imaging of Anesthesia-Specific Alterations in Microglial Surveillance and Photodamage-Directed Motility in Mouse Cortex. Front Neurosci 13, 421.
Szepesi, Z., Bijata, M., Ruszczycki, B., Kaczmarek, L., Wlodarczyk, J., 2013. Matrix metalloproteinases regulate the formation of dendritic spine head protrusions during chemically induced long-term potentiation. PLoS One 8, e63314.
Tzioras, M., Daniels, M., King, D., Popovic, K., Holloway, R., Stevenson, A., Tulloch, J., Kandasamy, J., Sokol, D., Clare, J., Smith, C., Miron, E., Henstridge, C., McColl, B., Spires-Jones, T.L., 2019. Altered synaptic ingestion by human microglia in Alzheimer's disease. bioRxiv 795930.
Wake, H., Moorhouse, A.J., Jinno, S., Kohsaka, S., Nabekura, J., 2009. Resting microglia directly monitor the functional state of synapses in vivo and determine the fate of ischemic terminals. J. Neurosci. 29, 3974–3980.
Wang, C., Yue, H., Hu, Z., Shen, Y., Ma, J., Li, J., Wang, X.D., Wang, L., Sun, B., Shi, P., Wang, L., Gu, Y., 2020 Feb 7. Microglia mediate forgetting via complement-dependent synaptic elimination. Science 367 (6478), 688–694.
Weinhard, L., di Bartolomei, G., Bolasco, G., Machado, P., Schieber, N.L., Neniskyte, U., Exiga, M., Vadisiute, A., Raggioli, A., Schertel, A., Schwab, Y., Gross, C.T., 2018. Microglia remodel synapses by presynaptic trogocytosis and spine head filopodia induction. Nat. Commun. 9, 1228.
Wright, A.L., Zinn, R., Hohensinn, B., Konen, L.M., Beynon, S.B., Tan, R.P., Clark, I.A., Abdipranoto, A., Vissel, B., 2013. Neuroinflammation and neuronal loss precede Aβ plaque deposition in the hAPP-J20 mouse model of Alzheimer's disease. PLoS One 8, e59586.
Wu, T., Dejanovic, B., Gandham, V.D., Gogineni, A., Edmonds, R., Schauer, S., Srinivasan, K., Huntley, M.A., Wang, Y., Wang, T.M., Hedehus, M., Barck, K.H., Stark, M., Ngu, H., Foreman, O., Meilandt, W.J., Elstrott, J., Chang, M.C., Hansen, D. V., Carano, R.A.D., Sheng, M., Hanson, J.E., 2019. Complement C3 Is Activated in Human AD Brain and Is Required for Neurodegeneration in Mouse Models of Amyloidosis and Tauopathy. Cell Rep. 28, 2111–2123.e2116.
Wu, Y., Dissing-Olesen, L., MacVicar, B.A., Stevens, B., 2015. Microglia: Dynamic Mediators of Synapse Development and Plasticity. Trends Immunol. 36, 605–613.
Wu, X., Fu, Y., Knott, G., Lu, J., Di Cristo, G., Huang, Z.J., 2012 Jan 4. GABA signaling promotes synapse elimination and axon pruning in developing cortical inhibitory interneurons. J Neurosci 32 (1), 331–343.
Xin, Y.R., Jiang, J.X., Hu, Y., Pan, J.P., Mi, X.N., Gao, Q., Xiao, F., Zhang, W., Luo, H.M., 2019 Nov. The Immune System Drives Synapse Loss During Lipopolysaccharide-Induced Learning and Memory Impairment in Mice. Front. Aging Neurosci. 15 (11), 279.
Zhao, J., Bi, W., Xiao, S., Lan, X., Cheng, X., Zhang, J., Lu, D., Wei, W., Wang, Y., Li, H., Fu, Y., Zhu, L., 2019. Neuroinflammation induced by lipopolysaccharide causes cognitive impairment in mice. Sci. Rep. 9, 5790.
Yona, S., Kim, K.W., Wolf, Y., Mildner, A., Varol, D., Breker, M., Strauss-Ayali, D., Viukov, S., Guilliams, M., Misharin, A., Hume, D.A., Perlman, H., Malissen, B., Zelzer, E., Jung, S., 2013 Jan 24. Fate mapping reveals origins and dynamics of monocytes and tissue macrophages under homeostasis. Immunity. 38 (1), 79–91.
Velez-Perez, A., Holder, M.K., Fountain, S., Blaustein, J.D., 2020 Jul 2. Estradiol Increases Microglial Response to Lipopolysaccharide in the Ventromedial Hypothalamus during the Peripubertal Sensitive Period in Female Mice. eNeuro. 7 (4). ENEURO.0505-19.2020.
Guo, J.L., Narasimhan, S., Changolkar, L., He, Z., Stieber, A., Zhang, B., Gathagan, R.J., Iba, M., McBride, J.D., Trojanowski, J.Q., Lee, V.M., 2016 Nov 14. Unique pathological tau conformers from Alzheimer's brains transmit tau pathology in nontransgenic mice. J Exp Med. 213 (12), 2635–2654.
Holtmaat, A., De Paola, V., Wilbrecht, L., Knott, G.W., 2008 Sep 1. Imaging of experience- dependent structural plasticity in the mouse neocortex in vivo. Behav Brain Res. 192 (1), 20–25.
Holtmaat, A., Wilbrecht, L., Knott, G.W., Welker, E., Svoboda, K., 2006 Jun 22. Experience-dependent and cell-type-specific spine growth in the neocortex. Nature. 441 (7096), 979–983.
Young, K., Morrison, H., 2018 Jun 5. Quantifying Microglia Morphology from Photomicrographs of Immunohistochemistry Prepared Tissue Using ImageJ. J Vis Exp. 136, 57648.